POLITECNICO DI TORINO

Master Degree in Biomedical Engineering

Politecnico di Torino

NTNU

Norwegian University of Science and Technology

Graph-based algorithms for the analysis of functional connectivity in zebrafish habenula and telencephalon

Supervisor
Prof. Valentina Agostini

External supervisor
Prof. Emre Yaksi

Candidate
Caterina Putti
279929

Academic Year 2020/2021

Abstract

The human brain is a huge and complex network in which smaller structures communicate and process information at different scales of time and space. In recent years brain connectivity has become one of the main interests of many leading neuroscience centres all over the world, which investigate different aspects of brain connectivity, in particular the branch called functional connectivity, for many different purposes: from clinic applications in neurological diseases, to basic research both on humans and on experimental models. As a matter of fact, animal models allow the study of much simpler brain networks and structures compared to humans, and they open the possibility to exploit imaging or genetic tools which can't be performed on humans for technical or ethical reasons. Yaksi lab, the laboratory within which this study has been carried out, is a research centre in the field of systems neuroscience, in which neuroscientists, physicists and engineers are interested in how behavioural tasks and sensory computation affect the neural circuits and pathways within the brain of zebrafish. These animal models allow two-photon calcium imaging, an imaging tool which records fluorescence signals related to the activation of single neurons. Two of the main brain areas the lab has been interested in are telencephalon, the homolog of mammalian amygdala and hippocampus, and habenula, which can be found also in mammals. The aim of this thesis is to investigate two aspects, related to spatial and temporal organization respectively, of functional connectivity in these two zebrafish brain regions, exploiting some graph-based algorithms that, as confirmed in literature, are particularly suitable for representing and visualizing brain networks. On one hand, a spectral clustering algorithm was implemented to cluster synchronous neurons during ongoing activity. A heuristic method was used to estimate the optimal number of clusters, but it resulted in a poor ability to recognize small clusters. On the other hand, the temporal development of neural activation and its changing between ongoing activity and odour stimulation were analysed, leading to clues on how different telencephalon and habenula are in terms of plasticity and learning behaviours.

Acknowledgments

First, I would like to thank Emre, Professor Yaksi for the Italians, for being such a good mentor. Your enthusiasm and your suggestions have guided me in this exciting but difficult and virtual experience, and you will always be a role model for me. Thanks to all the people from Yaksi lab, it was a pleasure to share a little piece of science with you.

Ringrazio la Professoressa Agostini per avermi dato la possibilità di tentare questa esperienza in un momento così delicato, e per il supporto mostratomi quando ne ho avuto bisogno.

Grazie a mamma, papà, Stefano, e pure a Francesco. Grazie alla nonna Egle e alla nonna Teresa. Sono orgogliosamente brandelli della mia famiglia.

Grazie, anzi… Thanks to Anna and Giorgia, without you I would never have been able to achieve this feat. E grazie alla Mari, per cui vale lo stesso, ma in italiano.

Grazie a Lori per aver scelto strumentazione ed essersi condannato ad altri due anni insieme. Non avrei potuto chiedere di meglio.

Grazie alle mie amiche di Torino, giovani e vegliarde.

Grazie (a colori) alle mie persone di sempre.

Table of contents

1 Introduction

1.1 Brain connectivity

Starting with Camillo Golgi and Ramon y Cajal, the two fathers of neuroscience, countless studies were carried out to get a little closer to understanding the human brain: the most complex and perfect engine that has ever existed. This powerful organ is made up of about 100 billion (10^{11}) neurons connected by about 100 trillion (10^{14}) synapses, and this huge network is anatomically and functionally organized over different scales of time and space. For the time being we know very little about how this highly connected network could affect and be the driving force of every movement, thought, feeling and behaviour we as human beings are able to produce.

1.1.1 Paradigms of systems neuroscience

Systems neuroscience is the branch of neuroscience that actually investigates the structure and dynamics of neural circuits and systems, focusing on how sensory information and external world perception are analysed within the brain. It is widely accepted that the brain processes information throughout the two fundamental principles of integration and segregation [1], which means that all the stimuli coming from sensory organs must be combined and then used to plan the next action. Integration is the ability to combine and merge the incoming stimuli, while segregation allows the splitting of information towards separate modules, which perform specialized local computations.

1.1.2 Types of brain connectivity

One of the major focuses of the earliest years in systems neuroscience is of course brain connectivity, which studies links and interactions between distinct units within brain [2] trying to understand brain mechanisms and organizational features under the efficient brain information processing, not only in humans but also in animal models. Based on the scale of the unit and the nature of the link one is interested in, brain connectivity is divided into three different types of connectivity, as schematically depicted in *Figure 1*:

- Structural or anatomical connectivity refers to synapses, the physical wirings between single neurons. These connections could link neighbour neurons as well as neurons physically placed in distant brain regions, and all together they

form white matter, which could be described by the *connectome* [3]. Anatomical connections are relatively stable within short time scales (seconds to minutes), but not for longer periods due to morphological change and synaptic plasticity.

- Functional connectivity is operationally described as the temporal correlation between spatially remote neurophysiological events [4]. It refers to synchronism which characterizes the activation of distinct neurons or more generally of diverse brain areas also distant from each other. Change at this level of connectivity occur over the sub-second time scale.
- Effective connectivity represents the influence one neural system exerts over another [4], and it directly reminds causal relationships existing between neurons or different brain areas. As functional connectivity effective connectivity varies rapidly over seconds or sub-seconds.

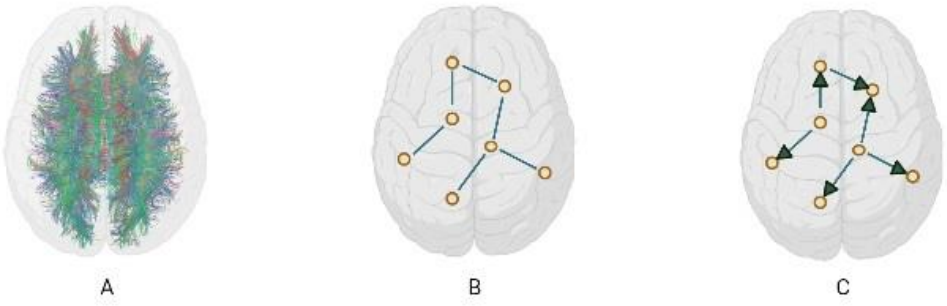

Figure 1: Schematic of the types of brain connectivity. (A) Structural connectivity. (B) Functional connectivity. (C) Effective connectivity.

1.1.3 State of the art for the analysis of brain connectivity

The study of brain connectivity is closely linked with the progress of neuroimaging techniques, both *in vitro* and *in vivo*. For example, in recent years new and promising results have been achieved in the field of structural connectivity thanks to diffusion tensor imaging (DTI), a non-invasive magnetic resonance imaging (MRI) method for visualizing location and orientation of fibres within the white matter [5][6]. It has to be mentioned that DTI suffers from very poor spatial resolution, but it could be a promising tool compared to other invasive axonal tract tracing method [7]. On the other hand, functional and effective connectivity refer to an abstract concept with no clear relation to physical connectivity, and so traditional imaging tools have been used combined with computational methods able to identify such temporal and causal relationships. Functional connectivity, in both healthy and diseased human brain, is probably the most studied aspect of brain connectivity, and it has been estimated from neuroimaging modalities like electroencephalogram (EEG) [8], magnetoencephalogram (MEG) [9], positron emission tomography (PET) [10], single-photon emission computed tomography (SPECT) [11] and functional magnetic resonance imaging (fMRI) [12][13]. fMRI is the predominant technique, and studies neural activation through the indirect blood-oxygen-level-dependent (BOLD) signal [14]. On animal models, other optical imaging techniques are available, mainly exploiting fluorescence calcium indicators. It is the case of Crame*r et al.* [15] who performed *in vivo* widefield calcium imaging on mice, Mann *et al.* [16] who used drosophila, and Avitan *et al.* [17] and Diaz Verdugo *et al.*[18], the latter from Yaksi Lab, who carried out two-photon calcium imaging on zebrafish. Computational methods to quantify functional connectivity in literature are usually divided into knowledge-based, which require prior knowledge about brain areas involved in the activation and make usually use of correlation-based metrics like cross-correlation or statistical parametric mapping [19], and, more often, data-driven approaches which aim to analyse activation signals through decomposition or clustering techniques. The most popular decomposition methods are principal component analysis (PCA) [10], independent component analysis (ICA) [20] and singular value decomposition (SVD) [21], while as clustering tools researchers mostly apply hierarchical clustering [22], fuzzy clustering [23] and spectral clustering [24]. Effective connectivity is probably the most difficult aspect to investigate in the field of brain connectivity, as one can see it as the

union of both structural and functional connectivity. The most important feature is the causal relationship that characterizes it, whereby so far it has been investigated with the same imaging tools as functional connectivity but using computational methods that emphasize such causal links. According to Granger causality (GC) one time series causes another one if the information contained in the first helps to predict the second, while dynamic causal modelling (DCM) estimates the coupling among brain areas and how it is influenced by environmentally changes. Both techniques have been applied to fMRI [25][26] giving some clues on direct interactions between brain regions during behavioural and cognitive tasks. An approach which can be used to analyse and visualize brain connectivity, and that can be applied in parallel to all the other mentioned approaches, is graph theory. Intuitively graphs or networks are particularly suitable for representing or modelling brain connectivity, and many examples can be found in literature [27][28][29]. Moreover, there are many helpful tools one can borrow from graph theory for analysing and quantifying brain connectivity aspects. Some of these mathematical methods are indeed used in this thesis, so the reader can find a quite comprehensive introduction of graph theory with focus on the aspect of spectral graph theory in the following chapters.

1.2 Zebrafish as a model in systems neuroscience

1.2.1 Experimental models

In all areas of experimental sciences "models are used to represent complex problems in simplified forms" [30], and they could be a powerful tool for investigating complex systems, at different level of complexity. There are three different types of models:

- *in vitro* models include cultures of cells or biological molecules outside their normal biological environment
- *in silico* models don't require the use of biological material, and computers are developed to model experiments or processes typical of biological world
- *in vivo* models are the ones performed on living organisms, usually animals, both humans and other animal species

Based on the field of research and the investigation to perform each of these models has advantages and disadvantages, and in neuroscience all the three are extremely promising.

In particular, in systems neuroscience *in vivo* animal models are the most common ones, due to the difficulties to reproduce both *in vitro* and *in silico* such a complex and interconnected structure as the brain is, and because they allow for a direct observation of the animal behaviour in response to specific stimuli. Even though mice and rats are the most popular animals used in research, zebrafish have become increasingly used during the past 30 years [31].

1.2.2 Zebrafish identity card

The zebrafish (*Danio rerio*) is a small tropical fish, belonging to the class of teleosts, the largest and most diverse group of vertebrates. His genome was sequenced in 2013 [32], and it was interestingly shown that approximately 70% of human genes have at least one zebrafish orthologue [32]. In their larval and juvenile stages zebrafish are transparent, which allows optical imaging techniques, and they are also suitable for a wide range of genetic approaches. Furthermore, they are small (up to 4 cm in length) and robust, cheaper to maintain than other vertebrate models, they produce an average clutch of 100-200 eggs per day and their generation time is short (3-4 months), which makes studies on their development easy to carry out. Indeed, all major organs develop already within 36 hours from fertilization, the hatching occurs on the third day and larvae show food seeking and avoidance behaviour already 2-3 days after hatching, i.e. around 5 days post fertilization (dpf) [33]. They also have the advantage to allow high-throughput approaches, much cheaper and faster compared to traditional techniques which is fundamental especially in the field of neuroscience [34]. Zebrafish are currently used for a wide range of research, but they are particularly interesting for behavioural studies which investigate the sensory and motor systems of the animals [35][36][37], as much as the ability to perform more complex tasks such as associative learning or active avoidance and fear conditioning [38][39][40].

1.2.3 Brain anatomy of zebrafish: telencephalon and habenula

A representation of the adult zebrafish brain is shown in *Figure 2*. Anatomically mammals' neurological structures are well-preserved in teleosts like zebrafish [41] and many similarities can be found, except for a big difference regarding the formation process of the ventricles: in mammals they arise from evagination, while in zebrafish from eversion [42]. Despite this, zebrafish telencephalon contains homologous of limbic

regions in mammals, as observed by Lal *et al.*[43]: the medial zone of dorsal telencephalon (Dm) is the homolog of the mammalian amygdala whereas the lateral part of dorsal telencephalon (Dl) is the functional equivalent of the hippocampus. Another interesting area which plays an important role in sensory information processing, learning behaviours and diseases like depression or addiction [44] is the habenula (Hb), an evolutionarily conserved diencephalic nucleus which can be found both in mammals and zebrafish [44]. It is divided in two principal subdomains which are zebrafish dorsal (dHb) and ventral habenula (vHb), the homologous to mammalian lateral and medial habenula, respectively. Habenula is a central hub connecting forebrain regions to midbrain units; it receives input from prefrontal cortex, thalamus and hypothalamus and has efferent connections towards interpeduncular nucleus and raphe nuclei [45], as depicted in *Figure 3*.

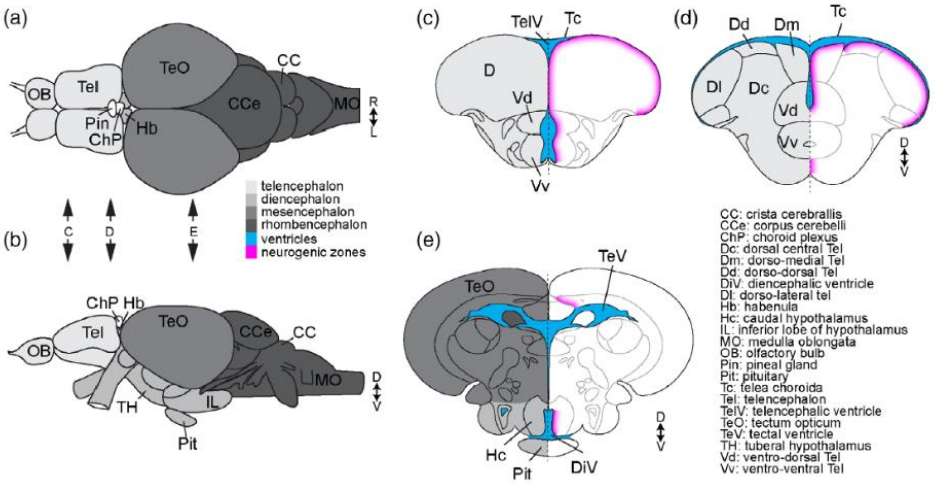

Figure 2: Schematic representation of the adult zebrafish brain seen from dorsal (a), lateral (b), or transverse (c-e) views. Brain areas represented in different shades of grey, ventricles in blue and neurogenic zones un magenta. (c-e) Transverse sections related to the C-E indicated sections. R: right, L: left, D: dorsal, V: ventral. From N. Jurisch-Yaksi at al. (2020) [46]

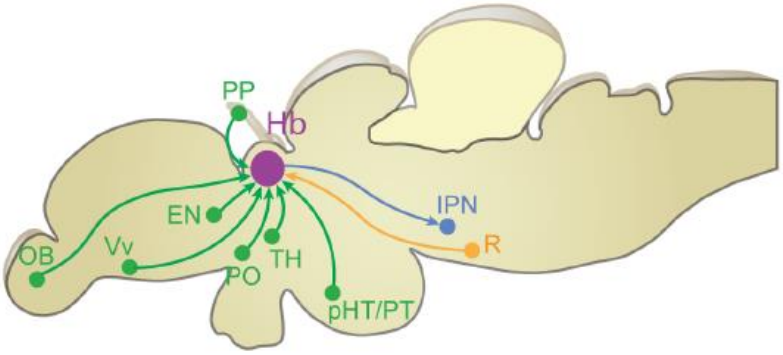

Figure 3: Schematic overview of habenula's afferent and efferent pathways. Sagittal view of the zebrafish brain. Green: afferent. Blue: efferent. Yellow: bidirectional connections. Hb: habenula. OB: olfactory bulb. Vv: ventral area of the subpallium. EN: enterpeduncular nucleus. PP: parapineal organ. PO: preoptic area. TH: thalamus. pHT/PT: posterior hypothalamus/posterior tuberculum. IPN: interpeduncular nucleus. R: raphe. From S. Fore et al. (2017) [44]

Aim of the work

This thesis has been carried out in collaboration with the Yaksi lab, a Norwegian neuroscience laboratory that performs, among others, functional connectivity analysis on zebrafish brain. Researchers make daily use of well-established computational tools performing operations as clustering neurons, visualizing brain networks and neural activity. The aim of this work is to further investigate some aspects of functional connectivity still unexplored for the majority of the lab members, exploiting graph-based algorithms that are particularly suitable for brain connectivity analysis. The investigations took two main directions:

- Spatial organization: neural assemblies during ongoing activity were examined through spectral clustering algorithm with the challenging goal of trying to provide a method for estimating the number of clusters, which is always a delicate aspect in most clustering algorithms.
- Temporal organization: the diversity of neural activation switching between ongoing and odour stimulated activity was explored thanks to a change of prospective which helps to follow the network development during these two different cognitive tasks.

1.3 Lab work

Yaksi lab is an interdisciplinary laboratory within the Kavli Institute for Systems Neuroscience at NTNU in Trondheim, Norway. The Institute is a leading research centre in the field of systems neuroscience, and, within it, Yaksi lab focuses on how sensory information is encoded in the brain and how it is modulated by learning and by internal brain states. Researchers in the lab mainly use zebrafish as animal models and apply a combination of functional imaging, optogenetics, molecular genetics and electrophysiological recordings in order to understand fundamental principles underlying the function and development of animal neural circuits. The lab has three major research lines: one investigates sensory computation, another is interested in the role of cilia in brain development and function and the last one studies neural circuit mechanisms underlying neurological disease such as epilepsy. With regard to sensory computation, the branch this thesis focuses on, different brain areas and how they regulate behavioural

and sensory tasks are investigated: indeed, during the past years habenula has been one of the main focuses of the lab. Many papers have been published about this topic from authors from the lab, and one of these was the starting point for this thesis. [47]

1.4 Our and my contribution

Unfortunately, due to the Covid pandemic, it was not possible for me to go to Norway and to participate in experiments and lab life. For this reason, I was kindly provided with the material from past experiments by Emre Yaksi and Ewelina Bartoszek. The dataset consisted of neuronal fluorescence traces already extracted from two-photon calcium imaging recorded on habenula and telencephalon of three juvenile zebrafish during ongoing activity and odour stimulation. I was not able to participate in the experimental procedures of fish maintenance and two-photon microscope recordings, therefore Bartoszek and colleagues took care of the extraction of fluorescence traces from recordings applying well established methods for image alignment and cell detection, previously validated and published by the lab itself.

I personally took care of all the analysis performed on the data. I made the decision on what kind of further investigations to perform on the provided dataset, with the constant supervision and suggestion of Professor Emre Yaksi. All the algorithms and the statistical tests were implemented in MATLAB®.

1.5 Outline

This first chapter provides a comprehensive introduction on what are brain and functional connectivity, on the animal models used for this study and on the objectives and the contributions of this thesis. The rest of this manuscript is organized as follows. In the second chapter, the materials and the methodologies used by scientists within the lab will be presented. The third chapter will focus on the mathematical aspects of the employed graph-based algorithms, the application of which will be explained in the fourth chapter together with the obtained results. In the fifth and last chapter, the results will be finally discussed and contextualized, and possible future studies will be presented.

2 Materials used in the lab

2.1 Calcium imaging

Calcium imaging is an optical microscopic technique widely used in many neuroscience laboratories in order to record neural activity both *in vitro* and *in vivo*. The fundamental assumption is that calcium is an indicator of cell activity, because of the Ca^{2+} ions flow entering the neuron during a depolarization event. So, if fluorophores calcium indicators are present within the cells the recorded fluorescence signals relate to the spiking electrical activity. There are two main classes of calcium indicators: chemical indicators, which are fluorescent dyes that bind and label calcium, and genetically encoded calcium indicators, which allow the creation of transgenic animal lines expressing the fluorescent protein. Yaksi lab makes use of two-photon excitation microscopy to record fluorescence signals on transgenic zebrafish lines, which express genes encoding a genetically encoded calcium indicator called GCaMP. The setup used in the lab allows the recording of neural activity with a resolution of single neurons in awake behaving animals.

2.2 Two-photon excitation microscopy

Single-photon and two-photon excitation microscopy are fluorescence imaging tools which exploit the ability of a fluorophore to absorb and emit photons. In single-photon excitation a fluorophore at a ground state S_0 can absorb a single photon which excites the fluorophore to a higher energy state S_1; then the fluorophore relaxes back to S_0 resulting in the emission of a fluorescence photon of light. The excitation photon must have a wavelength λ_{1p} related to the energy gap between the two states:

$$E_{S_1} - E_{S_0} = \frac{hc}{\lambda_{1p}} \qquad (1)$$

where h is the Plank constant and c the speed of light. Two-photon excitation arises from the same physical principle but it requires the simultaneous absorption of two photons, each carrying half of the energy with respect to single-photon excitation. In this way the wavelength of the two exciting photons λ_{2p} must be twice that of single-photon excitation ($\lambda_{2p} = 2\,\lambda_{1p}$) to fill the same energy gap, and it typically results in an excitation laser

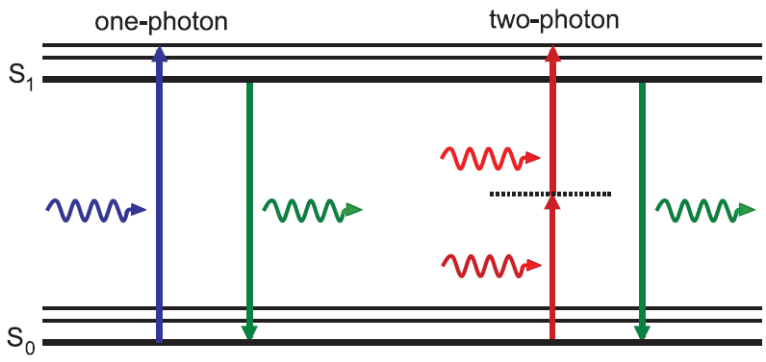

Figure 4: Physical principles of single-photon (left) and two-photon (right) excitation. From R. K. P. Benninger and D. W. Piston (2013) [48]

beam within the infrared spectrum. A schematic of the two physical principles is shown in *Figure 4*, where it can be seen that emission spectrum is related only to the energy gap between the two states and not to the exciting beam wavelength. The enabling technology for the two photon microscopy is an extremely powerful laser which generates an ultra-short pulsed laser beam, needed to ensure a photon flow high enough to increase the likelihood that two photons impact on the fluorophore at exactly the same time (within 10^{-18} s). [48] In addition, the laser beam is focused through a high numerical aperture (NA) objective, which leads to the high density of photons in a specific region called focal plane. From the outside, it is negligible that two-photon absorption occurs and virtually no fluorescence is generated. Two-photon excitation microscopy allows the recording of either single plane or volumetric regions, the latter often with a lower acquisition rate. With respect to single-photon or confocal microscopy, two-photon excitation microscopy has three main advantages. On one hand, it achieves imaging of extremely thick sections focusing the laser beam precisely on the focal plane. On the other hand, the infrared light typical of the excitation laser suffers less scattering than the blue light usually used in conventional microscopy, and it ensures a wide degree of separation between excitation and emission wavelengths, minimizing the spectral overlap between excitation and emission beams.

The recordings for the provided dataset were made with a two-photon microscope (Scientifica) equipped with a 16x water immersion objective (Nikon, NA 0.8, LWD 3.0,

plan). A mode-locked Ti:Sapphire laser (MaiTai Spectra Physics) tuned to 920 nm provided the pulsed (about 80 million pulses per second) laser beam for excitation, and recordings were performed as volumetric (5-7 planes with a Piezo (Physik Instrumente (PI)) with an acquisition rate of 2.64 Hz (average image size 1536 x 750 pixels). The microscope set up can be seen in *Figure 5*.

Figure 5: Two-photon microscope set up from the Yaksi lab.

2.3 Transgenic zebrafish lines and maintenance

Zebrafish used for this study were three juvenile animals (3 to 4 weeks old) and analysed irrespective of their gender. For two-photon calcium imaging in the lab Tg(elavl3:GCaMP5) [49], Tg(elavl3:GCaMP6s) and Tg(elavl3:GCaMP6s-nuclear) [50] zebrafish lines are used, which express panneuronally GCaMP5s, GCaMP6s and nuclear GCaMP6s respectively. GCaMP is a family of genetically encoder calcium indicators that when bound to Ca^{2+} fluorescence green approximately with a peak excitation wavelength of 480 nm and a peak emission wavelength of 510 nm [51]. For this reason, the excitation laser beam wavelength for two-photon excitation microscopy was tuned to 920 nm.

NFSA (Norwegian Food Safety Authority) has approved the animal facility and fish maintenance. Fish within the lab were kept in 3,5 L tanks in a Tecniplast ZebTec Multilinking System with constant conditions (28.5 °C, pH 7.2, 700 mSiemens, 14:10 h light/dark cycle). Dry food (SDS 100 up to 14 dpf and SDS 400 for adult animals, Special Diets Services, Tecnilab BMI, the Netherlands) was given to fish twice a day, in addition to Artemia nauplii (Grade 0, Platinum Label, Argent Laboratories, Redmond, USA) once a day. From fertilization to 3 dpf larvae were kept in a Petri dish with egg water (1.2 g marine salt in 20 L reverse osmosis (RO) water, 1:1000 0.1% methylene blue) and between 3 and 5 dpf in artificial fish water (AFW: 1.2 g marine salt in 20 L RO water).

2.4 Experimental procedure

Recordings were performed during a period of approximately 13 minutes and include a first period of ongoing activity, three odour stimulations of 30 seconds each alternated with periods of no stimulation, and another period of ongoing activity, as schematically reported in *Figure 6*.

For in vivo imaging, fish were embedded in 2 - 2.5 % low-melting-point agarose (LMP, Fisher Scientific) in a recording chamber (Fluorodish, World Precision Instruments). To ensure odour to reach the nostrils, the LMP agarose was removed carefully in front of the nose, after solidifying for 20 minutes. The constant perfusion of AFW bubbled with carbogen (95 % O_2 and 5 % CO_2) was maintained during the experiment. The odour stimulations were performed with high performance liquid chromatography (HPLC) injection valve (Valco Instruments) controlled with Arduino Due.

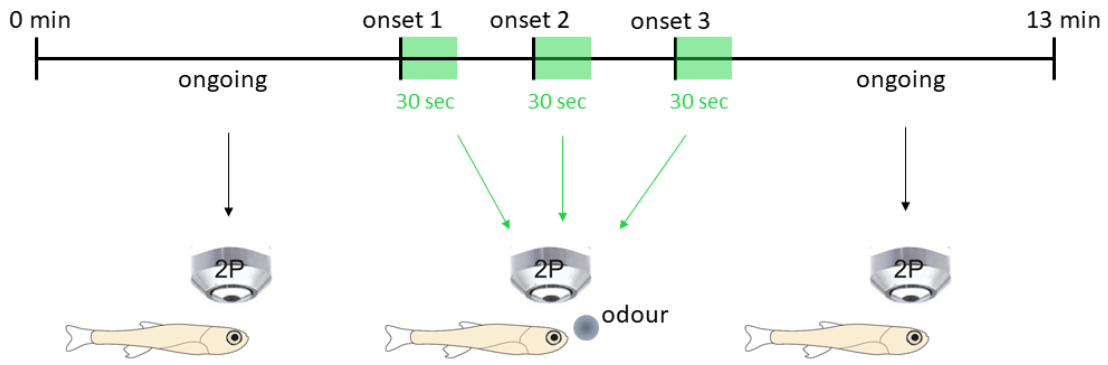

Figure 6: Schematic of the experimental procedure. The three onsets are the odour stimulation onsets, the three green panels are the odour stimulation of 30 seconds each. 2P: two-photon microscope. Adapted from Bartoszek et al.(2021) [47]

Before each experiment, a trial with fluorescein (10^{-4} M in AFW) was performed to determine precise onset of odour delivery.

2.4.1 Odour preparation

Odour panel used in the lab consists of food odour (1g/50ml dilution), skin extract (1g/50ml dilution), urea (10^{-4} M), bile-acid mixture (taurocholic acid, taurodeoxycholic acid at $5x10^{-4}$ M), amino acid mixture (Alanine, Phenylalanine, Methionine, Histidine, Cysteine, Arginine, Glutamic acid at 10^{-4} M), and ammonium chloride (10^{-4} M). All odorants were purchased from Sigma Aldrich. Food odour was prepared using commercially available fish food: 1 g of food particles was incubated in 50 ml of fish water (FW) for at least 1 h, filtered through filter paper, and diluted to 1:50. For skin extract [52] adult zebrafish were first euthanized in ice-cold water and decapitated, the skin was peeled off from the body. 1g of skin was incubated in 2 ml of AFW and was vortexed at 1300 rpm for 1 h at 4 °C. After, the skin extract was dissolved in 50 ml of AFW and filtered through the filter paper. All odours were prepared from the frozen stocks immediately before use.

2.5 Provided dataset extraction

Two-photon microscopy extracted images were aligned using a well-established method described in [53][18]. Recordings were then visually inspected for remaining motion and vertical drifts, and the ones with motion artifacts were discarded. Regions of interest (ROIs) corresponding to neurons were automatically detected using a template matching algorithm [49][18] and visually confirmed. To calculate the time trace of each neuron, pixels belonging to each ROI were averaged over time. For each ROI, fractional change in fluorescence ($\Delta F/F$) relative to baseline was calculated.

Ultimately, the provided recordings come from telencephalon and habenula of three fish during approximately 13 min of ongoing activity with three odour stimulation periods. For each fish brain region, the dataset is made up of a data matrix with neurons along the rows, time samples along the columns and $\Delta F/F$ as entries, the neurons spatial coordinates and the three odour onsets.

3 Basis of graph theory and spectral graph theory

Graph theory is an extremely wide branch of modern mathematics and has become increasingly popular over the last decades. Here the foundations for the understanding of the mathematical methods applied in this thesis will be laid, which are only a small part of possible notions and definitions. They will cover basic definitions of a graph, how to construct a graph from data and some typical graph properties involving a special matrix called Laplacian, which are referred as spectral properties: a clustering tool and a method for drawing the graph. The two distance measures used to assess distance between nodes within a graph are then explained.

3.1 Definition of a graph

A graph G is an intuitive mathematical structure which aims to represent the pairwise relation between objects within a typically 2D or 3D drawing. It consists of a set of n finite number of these objects, called vertices $V = \{v_1, \dots, v_n\}$ (or nodes), linked by a set of edges E which represent the relations between vertices, and it is indicated by $G = (V, E)$. Within the drawing vertices are depicted by circular points, labelled often by numbers or letters, and edges by line connecting two vertices. The edges can be both unweighted and weighted, meaning that the strength of the relation can be modulated by a weight. In an unweighted graph all the edges are equally heavy, and conventionally weighted by ones.

Based on the type of relation which can connect two vertices, graphs are divided into two big categories: undirected and directed graphs. In undirected graphs the relation doesn't have a direction and the link between two vertices indicates a two-way relationship. In the drawing it results in a simple line between the two nodes. On the other hand, in directed graphs for each edge there are a starting vertex and an ending one. The relation is indeed directed one-way oriented and it is depicted by an arrow between the two nodes. So undirected graphs are useful for all the cases in which the relationship to be modelled is symmetric while directed graphs are mostly used for the application characterized by a causal relation or a temporal ordering. Another definition is based on the number of edges allowed between two nodes: if more than one edge can link two different nodes the resulting graph will be a multigraph. There is also the possibility for self-loops to exist.

A self-loop occurs when a single edge, which could be both directed and undirected, connects a node to itself so that the starting vertex is also the ending one. If a graph is not a multigraph and does not have self-loops it is referred as simple graph. In this work only undirected simple graph will be used.

Ultimately the graph as the abstract and non-visual mathematical structure should not be confused with the drawing of the graph itself. There are infinite possible ways to visually represent the same graph because points and lines can be arranged in an infinite number of ways on a sheet of paper while the number of nodes and the structural connections between them remain exactly the same. Indeed, unless the coordinates of the nodes have a known geometric meaning, different layouts can be suitable for different purposes. Sometimes the axes of the graph do not even have much importance; often, as in the case of this work, the axes represent an arbitrary scale not directly related with any physical quantity, but which can be useful for defining some metrics or distances within the graph itself. The field of study interested in such layouts and representations is known as graph drawing. In this thesis, only one particular approach will be analysed in detail in the paragraph about spectral graph drawing.

3.2 Similarity graph

The idea of constructing a similarity graph with the elements of a dataset is widely used mainly with respect to clustering algorithms [54], but it could be a useful representation for many other different purposes. Given a set of n data points $x_1, \dots, x_n$ and a measure of pairwise similarity $s_{ij} \geq 0$ between all pairs of points x_i and x_j it is always possible to arrange them in a form of similarity graph $G = (V, E)$, in which vertices v are the n data points, and edges e between nodes exist and are weighted based on the pairwise similarity metric. In general, points x_i could be defined in a space of any dimensionality m $\mathbb{R}^m$, as long as the non-negative similarity measure s_{ij} exists. Often s_{ij} is defined starting from some well-known measure of pairwise distance d_{ij} between x_i and x_j, based on what data points actually represent such as Euclidean, Mahalanobis, Cosine or Correlation distance.

For the purposes of this thesis two distance measures are used in this context:

- Correlation distance:

$$d_{ij}^{CORR} = 1 - \frac{(x_i - \bar{x}_i)(x_j - \bar{x}_j)'}{\sqrt{(x_i - \bar{x}_i)(x_i - \bar{x}_i)'}\sqrt{(x_j - \bar{x}_j)(x_j - \bar{x}_j)'}} \tag{2}$$

$$\text{with} \quad \bar{x}_s = \frac{1}{n}\sum_t x_{st}$$

- Cosine distance:

$$d_{ij}^{COS} = 1 - \frac{x_i\, x_j{}'}{\sqrt{(x_i\, x_i{}')(x_j\, x_j{}')}} \tag{3}$$

It has been said that edges are related to similarities (or distances) but there could be different ways for modelling the local neighbourhood relations between data points. The most commonly used methods in literature to construct similarity graphs and assign edges are:

- ε-neighbourhood
- k-nearest neighbour
- fully connected graph

In a ε-neighbourhood graph two nodes are connected if the pairwise distance between them is smaller than a fixed radius ε (or the similarity is bigger than a certain threshold). This method requires a priori knowledge about the distance range that can be found between data points in order to fix the parameter ε. Since all the edges have the same scale given by ε, weights do not add much information to the graph so that this kind of graph is usually unweighted. k-nearest neighbour method connects vertex v_i to vertex v_j if v_j belongs to the group made up by the first k neighbours of v_i, in terms again of distance or similarity. However, in this way one should obtain a directed graph because the definition of neighbourhood is not symmetric. In order to make the graph undirected there are two possible solutions. One is to disregard the direction of the edges and to connect v_i and v_j if either v_j is neighbour of v_i or v_i is neighbour of v_j. In this way the

obtained graph is the so called complete k-nearest neighbour graph (often simply indicated as k-nearest neighbour graph). The second option, which leads to the mutual k-nearest neighbour graph, is to connect v_i and v_j if both v_j is neighbour of v_i and v_i is neighbour of v_j. This choice is obviously stricter than the first one, and it results in a smaller number of edges and a way less connected graph. The parameter k has to be fixed for both types of k-nearest neighbour graphs, and they are often reported with weighted edges because the scale is relative to the single vertex and more informative than in ε-neighbourhood graph. In a fully connected graph, each vertex is connected to all the others, and edges can be weighted by their similarities. This kind of graph does not require parameters to be set, but it is often uninformative because it actually does not model any neighbourhood unless the similarity function itself models local characteristics.

The question about what kind of similarity graph to use and how to construct it is not trivial, and it could depend on the application as well as on the type of dataset. The definition of the similarity function is fundamental, and it has to allow a good modelling of the local neighbourhood. A metric able to represent the short-range behaviour (between similar nodes) is recommended because often the long-range behaviour (between distant nodes) is not informative and useful for the local neighbourhood modelling. One possible definition of a pairwise similarity which cares about local similarities starting from pairwise distance is the Gaussian Similarity function

$$s_{ij} = \exp\left(-\frac{{d_{ij}}^2}{2\sigma^2}\right) \qquad (4)$$

defined in terms of distance d_{ij} and the parameter σ. Claims about how to select suitable values for the parameters are reported in [55] by Von Luxburg. The author advises to keep the Gaussian function simple setting σ equal to 1, and some rules of thumb for some typical parameters to assign when working with ε-neighbourhood and k-nearest neighbour graphs. In particular, for the first case he suggests choosing ε "as the length of the longest edge in a minimal spanning tree of the fully connected graph", while for the complete k-nearest neighbour case a good starting point is to set k equal to the natural logarithm of the number of nodes $\log(n)$. He admits that for the mutual k-nearest

neighbour graph, such rule of thumb does not exist and he suggests to choose k significantly larger than for the complete k-nearest neighbour one.

3.3 Graph notation

Let be $G = (V, E)$ an undirected, weighted graph made up of n vertices. In the following, vertices will be indicated as v_i, while the edge between vertices v_i and v_j will be referred as e_{ij}, with $i, j = 1, \dots, n$. Since the graph is weighted, we can associate the weight $w_{ij} \geq 0$ to the edge e_{ij}. If $w_{ij} = 0$ there is no edge connecting v_i to v_j. Furthermore, if the graph is unweighted all the following considerations remain valid with $w_{ij} = 1$ for each existing edge. Weights w_{ij} are the entries of the squared $n \times n$ adjacency matrix A of the graph, so that single elements of A will be:

$$A_{ij} = w_{ij} \qquad i, j = 1, \dots, n \tag{5}$$

For an undirected graph A is symmetric because it must be $w_{ij} = w_{ji}$.

In the case of similarity graph a natural way to see pairwise similarity measure s_{ij} between every pair of nodes is the so called similarity matrix S, simply defined as:

$$S_{ij} = s_{ij} \qquad i, j = 1, \dots, n \tag{6}$$

In this case the graph and so the adjacency matrix A can be obtained from S through one of the methods explained in the above subchapter 2.2, such that for example $A = S$ for a fully connected graph.

The degree of a vertex v_i is a measure of how much it is connected, and it is defined as:

$$d_i = \sum_{j=1}^{n} w_{ij} \tag{7}$$

It is possible to define a degree matrix D as the $n \times n$ diagonal matrix with $d_1, \ldots, d_n$ on the principal diagonal, so that:

$$D_{ij} = \begin{cases} d_i & i = j \\ 0 & i \neq j \end{cases} \qquad i, j = 1, \ldots, n \qquad (8)$$

An example of an undirected, unweighted simple graph with its relating adjacency and degree matrices is shown in *Figure 7*.

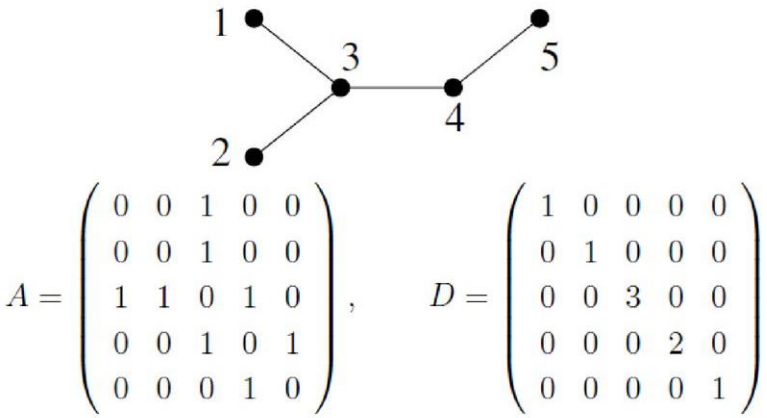

Figure 7: Adjacency matrix A and degree matrix D for an undirected, unweighted graph.

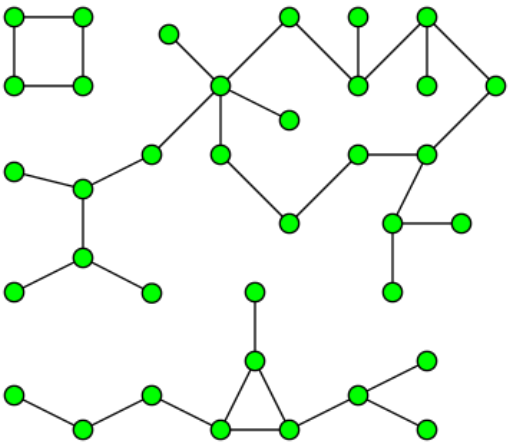

Figure 8: Undirected graph made up of 3 connected components.

The last useful definition to include is about connected component. Given a subset of vertices $Q \in V$, its complement $V \backslash Q$ it is denoted by $\bar{Q}$. The subset Q is called a connected component if each vertex within Q has at least one edges and there are no connections between vertices in Q and $\bar{Q}$ (*Figure 8*).

3.4 Graph Laplacians and spectral graph theory

Another important matrix for a graph is the graph Laplacian, which has an entire branch dedicated to the study of it, its eigenvalues and eigenvectors called spectral graph theory [56]. The name spectral comes simply from the fact that eigenvalues of a matrix are called its spectrum. Spectral decomposition (or eigendecomposition) of a diagonalizable matrix is a powerful algebraic tool for representing the matrix and some important related features; moreover, graph Laplacian can be seen as a sort of matrix representation of the discrete Laplacian algebraic operator, and because of this it brings along with it many interesting properties. The Laplacian matrix can also be used to construct low dimensional embeddings useful in a variety of applications. As expected, many authors have been extensively studying these topics, and a wide literature about graph Laplacian and its spectral properties can be found [56][57][58][59][60]. For the purposes of this thesis, only main definitions and few summarized major features of the graph Laplacian will be provided, so if the reader is interested in further insights about these topics the aforementioned literature will supply broad and detailed studies, from a purely mathematical and algebraic point of view.

For the sake of clarity many different definitions of Laplacian matrices exist in literature, based on the definition the author gives. Here the more common definitions of unnormalized and normalized Laplacian will be reported and discussed.

3.4.1 The unnormalized graph Laplacian

The unnormalized Laplacian of a simple graph is the squared $n \times n$ matrix defined as:

$$L = D - A \tag{9}$$

where D is the degree matrix and A is the adjacency matrix. From this simple definition the entries of the Laplacian L result in:

$$L_{ij} = \begin{cases} d_i & i = j \\ -w_{ij} & i \neq j \end{cases} \qquad i, j = 1, \dots, n \tag{10}$$

According to what has been said before, only some of the main features will be here reported:

- L is real and symmetric so its eigenvalues are real and eigenvectors orthogonal
- L is positive semi-definite and hence its eigenvalues are non-negative
- L has n real non-negative eigenvalues λ_i, such that $0 = \lambda_1 \leq \lambda_2 \leq \cdots \leq \lambda_n$
- 0 is the smallest eigenvalue of L, and the corresponding eigenvector is the constant one vector 1_n
- The multiplicity of the 0 eigenvalue is equal to the number of connected components of the graph G

3.4.2 The normalized graph Laplacians

The normalized graph Laplacian can be defined in two different ways which are often called the symmetric and the random walk Laplacian. Their definitions are, respectively:

$$L_{sym} = D^{-\frac{1}{2}} L D^{-\frac{1}{2}} = I - D^{-\frac{1}{2}} A D^{-\frac{1}{2}} \tag{11}$$

$$L_{rw} = D^{-1} L = I - D^{-1} A \tag{12}$$

Both are squared $n \times n$, but only L_{sym} is symmetric and hence the name. The random walk Laplacian L_{rw} derived from its definition: $D^{-1}A$ is indeed the transition matrix of a random walker on the graph, and it is related with the likelihood for a random walker to be located on a certain vertex.

Again, the main features of the two normalized Laplacian are summarized here:

- L_{sym} and L_{rw} are positive semi-definite and they both have n non-negative real eigenvalues $0 = \lambda_1 \leq \lambda_2 \leq \cdots \leq \lambda_n$
- λ is an eigenvector of L_{rw} with eigenvector u if and only if λ is an eigenvector of L_{sym} with eigenvector $w = D^{\frac{1}{2}} u$

- 0 is the smallest eigenvalue of both L_{sym} and L_{rw}; for L_{rw} its corresponding eigenvector is the constant one vector 1_n, while for L_{sym} the corresponding eigenvector is the vector $D^{\frac{1}{2}}1_n$
- For both L_{sym} and L_{rw} the multiplicity of the 0 eigenvalue is equal to the number of connected components of the graph G
- λ is an eigenvector of L_{rw} with eigenvector u if and only if λ and u solve the generalized eigen-problem $Lu = \lambda Du$

It is important to highlight the last property about the generalized eigen-problem, which establishes the possibility to derive eigenvectors of L_{rw} just solving the generalized eigenvalue problem $Lu = \lambda Du$.

3.5 Spectral clustering

Intuitively clustering aims to group together similar objects while dividing dissimilar ones. Many different algorithms have been developed for this purpose, and they are widely used in a large variety of fields such as biology, marketing, computers science and many others. Conventionally clustering algorithms are divided in categories depending on the notion of clusters they use; the most popular types of clustering algorithms can be divided in the following classes:

- Centroids-based clustering which includes the k-means algorithm
- Connectivity-based clustering like hierarchical methods
- Density-based clustering which discriminate dense region in the data space
- Fuzzy or soft clustering which introduce a likelihood of belonging to a cluster

As a matter of fact, these most popular classes don't include a wide variety of algorithms such as all the graph-based models or the subspace models, which slightly manipulate the data before applying a clustering algorithm, and spectral clustering fall right into this category.

Looking at the naïve definition of clustering given above referring to weighted similarity graph, one can easily translate clustering into partitioning the graph in such a way that edges between nodes belonging to the same cluster are heavier than edges connecting

nodes in different clusters. This is exactly what spectral clustering algorithms do, exploiting the possibility to arrange data within a graph and so the useful properties of the graph Laplacian, that can be both unnormalized and normalized. The most common spectral clustering algorithms mainly differ in what kind of Laplacian matrix they use, but they are substantially similar to each other. They exploit the change of representation of the information contained in the similarity graph allowed by the spectrum of the Laplacian, which can lead to a new reduced-dimensional representation that enhance the cluster-properties within the data. In this new space a simple k-means clustering algorithm can be applied in order to obtain indices for the final clusters. Because of the application of k-means algorithm, the number of clusters k must be known a priori and it is the only input, together with the similarity matrix obtained from data, of every spectral clustering algorithm.

Here a pseudocode for the three main spectral clustering algorithms will be reported, and a method which can be useful for estimating the number of clusters common to the three of them will be then explained. For the discussion of this topic reference is made to the milestone tutorial of von Luxburg [55], and the same notation introduced above will be adopted. From a dataset of n points $x_1, \dots, x_n$ to be clustered in $C_1, \dots, C_k$ clusters, and a measure of pairwise similarity s_{ij}, a similarity matrix $S \in \mathbb{R}^{n \times n}$ can be computed. S and the number of clusters k will be the only inputs for all the three algorithms. In the following there will be no explanation of the k-means clustering algorithm which will be taken for granted.

3.5.1 Unnormalized spectral clustering

Input: similarity matrix $S \in \mathbb{R}^{n \times n}$, number of clusters k

- Construct a similarity graph by one of the algorithms described in 3.2. Let A be its weighted adjacency matrix
- Compute the unnormalized Laplacian L
- Compute the first k eigenvectors $u_1, \dots, u_k$ of L
- Let $U \in \mathbb{R}^{n \times k}$ be the matrix containing the vectors $u_1, \dots, u_k$ as columns
- For $i = 1, \dots, n$, let $y_i \in \mathbb{R}^k$ be the vector corresponding to the i-th row of U

- Cluster the points $(y_i)_{i=1,\dots,n}$ in $\mathbb{R}^k$ with the k-means algorithm into clusters $B_1, \dots, B_k$

Output: clusters $C_1, \dots, C_k$ with $C_i = \{x_i | y_i \in B_i\}$

3.5.2 Normalized spectral clustering

Based on which version of normalized Laplacian is used, two different normalized spectral clustering algorithms exist and are usually used in literature.

According to Ng, Jordan and Weiss [61] who used symmetric normalized Laplacian the algorithm is made up of the following steps.

Input: similarity matrix $S \in \mathbb{R}^{n \times n}$, number of clusters k

- Construct a similarity graph by one of the algorithms described in 3.2. Let A be its weighted adjacency matrix
- Compute the symmetric normalized Laplacian L_{sym}
- Compute the first k eigenvectors $u_1, \dots, u_k$ of L_{sym}
- Let $U \in \mathbb{R}^{n \times k}$ be the matrix containing the vectors $u_1, \dots, u_k$ as columns
- Form the matrix $T \in \mathbb{R}^{n \times k}$ from U by normalizing the rows to 1-norm, that is set $t_{ij} = u_{ij} / (\sum_k {u_{ik}}^2)^{1/2}$
- For $i = 1, \dots, n$, let $y_i \in \mathbb{R}^k$ be the vector corresponding to the i-th row of U
- Cluster the points $(y_i)_{i=1,\dots,n}$ in $\mathbb{R}^k$ with the k-means algorithm into clusters $B_1, \dots, B_k$

Output: clusters $C_1, \dots, C_k$ with $C_i = \{x_i | y_i \in B_i\}$

On the other hand, Shi and Malik [62] implemented an algorithm in order to segment images, and the pseudocode of their algorithm is the following.

Input: similarity matrix $S \in \mathbb{R}^{n \times n}$, number of clusters k

- Construct a similarity graph by one of the algorithms described in 3.2. Let A be its weighted adjacency matrix
- Compute the unnormalized Laplacian L

- Compute the first k generalized eigenvectors $u_1, \dots, u_k$ of the generalized eigenproblem $Lu = \lambda Du$
- Let $U \in \mathbb{R}^{n \times k}$ be the matrix containing the vectors $u_1, \dots, u_k$ as columns
- For $i = 1, \dots, n$, let $y_i \in \mathbb{R}^k$ be the vector corresponding to the i-th row of U
- Cluster the points $(y_i)_{i=1,\dots,n}$ in $\mathbb{R}^k$ with the k-means algorithm into clusters $B_1, \dots, B_k$

Output: clusters $C_1, \dots, C_k$ with $C_i = \{x_i | y_i \in B_i\}$

This algorithm exploits the property about the generalized eigen-problem of L, so that the computed eigenvectors correspond to the eigenvectors of L_{rw}.

3.5.3 Estimation of the number of clusters

Spectral clustering exploits the properties of the graph Laplacian which are related to some interesting features of the graph such as the number of connected components. It has already been mentioned that the multiplicity of the null eigenvalue of the graph Laplacian is equal to the number of connected components within the graph, and this property holds for both the unnormalized and the two normalized Laplacians. Even in the case the graph is made up of a single connected component there is a useful tool called eigengap heuristic which compares the magnitude of the first eigenvalues in order to choose the optimal number of clusters k. The aim is to choose a k in such a way that the first $\lambda_1, \dots, \lambda_k$ are small if compared to the relatively larger eigenvalue λ_{k+1}. The first eigenvalue λ_1 will be 0 and all the eigenvectors will be sorted in ascending order because of the properties mentioned in 3.4, but this heuristic method looks for the first relatively important gap in the magnitude of the eigenvalues. For the justifications of this method reference is always made to [55], from which *Figure 9* is shown as example of the application of this method. The application of this heuristic procedure is quite struggling when clusters within the data are noisy or overlapping, and finding a well-defined gap on the eigenvalues distribution can be tricky and not always possible.

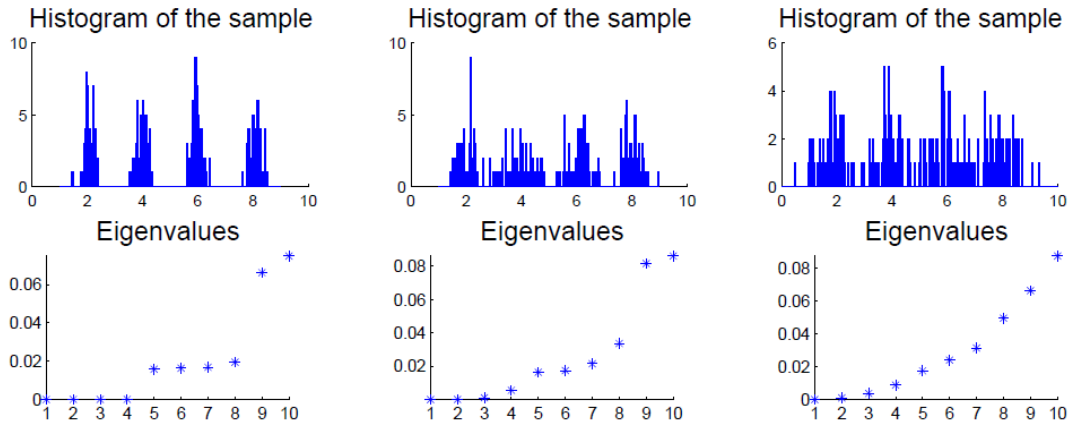

Figure 9: Example of eigengap heuristic method. Three synthetic datasets represented as histogram of the sample (above), and the plot of the first 10 eigenvalues of L_{rw} (under). The number of clusters is always 4, but the noise and the overlap between clusters increase from left to right. From U. Von Luxburg (2007) [55]

3.6 Spectral graph drawing: the eigen-projection in HDE subspace method

Graph drawing is the area of mathematics and graph theory focusing on the two-dimensional (sometimes three-dimensional) representation of a network. There are many conventional layout methods commonly used in literature such as force-based, spectral, orthogonal and layered. The branch of spectral graph drawing, or spectral layout, exploits the eigenvectors of the graph Laplacian, often manipulated by some algorithm, for obtaining axes for the drawing of the graph [63]. In this thesis the algorithm presented by Koren in [64] was used. Author argues that this new algorithm requires a very low computational time compared to others spectral algorithms, and it results in "nice" and faithful representations of the inner structure of the graph. This algorithm is a modification of the so called eigen-projection method firstly proposed by Hall [65] and explained in [64], and it requires first the construction of a high-dimensional embedding (HDE) subspace, then the eigen-projection of the coordinates of the nodes exploiting the graph Laplacian, allowing the final 2D visualization of the graph. The main advantage of this method is that, compared to the standard eigen-projection method, it needs calculating the first few eigenvectors of a squared matrix made up of fixed, as low as

desired, dimensions based on the subspace dimensions, instead of calculating them for the huge graph Laplacian of a graph with a high number of nodes.

The main two steps are here presented following the notation of [64] where n is the number of vertices in the graph, but forcing the final graph layout to be a 2-dimensional layout ($p = 2$ in [64]), defined by 2 vectors $x^1, x^2 \in \mathbb{R}^n$ where $x^1(i), x^2(i)$ are the two coordinates of the vertex v_i. This choice was made to improve readability and clarity of the following topics of which no mathematical proof will be given here. For further knowledge please see [64].

3.6.1 High-dimensional embedding (HDE) subspace

The high-dimensional embedding (HDE) is a sort of m-dimensional layout of the graph, with the number of dimensions m which can be chosen from the user, and it is made up of m axes $\chi^1, \dots, \chi^m \in \mathbb{R}^n$. For the construction of such embedding, m pivots vertices are selected by a heuristic for the k-centers problem, as explained in details in [64], so that they are uniformly distributed over the graph. Each χ^i is constructed by assigning to every j-th component, with $j = 1, \dots, n$, graph-theoretical distance between vertices v_i and v_j, which is defined as the length of the shortest path connecting the two nodes and is calculated using breadth-first-search (BFS) [66]. By construction, axis χ^i is related to the graph "point of view" of the i-th pivot vertex. The subspace obtained so far needs an orthonormalization process, achieved through a Gram-Schmidt procedure, leading the HDE subspace $\chi^1, \dots, \chi^m$ to form a valid basis. Finally, vectors are arranged column-wise building the $n \times m$ matrix χ.

3.6.2 Eigen-projection

This step is the one actually related to spectral properties of the graph Laplacian, and as general purpose it aims to project in a final space (in this case the 2D final drawing) graph nodes which are initially defined in a higher dimensional subspace exploiting the graph Laplacian. As many other graph drawing approaches also the eigen-projection can be seen as the solution of a constrained minimization problem, as shown in the reference by Koren [64]. In particular, the author manipulates the starting constrained minimization problem of the two vertex coordinates x^1, x^2 to the general form:

$$\min_{x^1,x^2} \frac{\sum_{k=1,2}(x^k)^T L x^k}{\sum_{k=1,2}(x^k)^T x^k} \qquad (13)$$

$$\text{subject to:} \quad (x^k)^T x^l = \delta_{kl} \qquad k,l = 1,2$$

$$(x^k)^T \cdot 1_n = 0 \qquad k,l = 1,2$$

in which L is the unnormalized graph Laplacian and δ_{kl} is the Kronecker delta which is defined as 1 if $k = l$ and 0 in all the other cases.

Moreover, he translates this information in the case he wants to optimize x^1, x^2 within the HDE subspace, replacing them with $\chi y^1, \chi y^2$, in which $y^1, y^2 \in \mathbb{R}^m$ are the two lowest eigenvectors (brief for eigenvectors of the two lowest eigenvalues) of the $m \times m$ matrix $\chi^T L \chi$. The new constrained minimization problem becomes the following:

$$\min_{y^1,y^2} \frac{\sum_{k=1,2}(y^k)^T \chi^T L \chi y^k}{\sum_{k=1,2}(y^k)^T y^k} \qquad (14)$$

$$\text{subject to:} \quad (y^k)^T y^l = \delta_{kl} \qquad k,l = 1,2$$

To briefly sum up the whole process, Koren achieves the two n-dimensional coordinates x^1, x^2 of the n graph vertices as following:

- Choosing m pivots vertices
- Constructing the $n \times m$ orthogonal matrix χ whose columns span the HDE subspace
- Computing y^1, y^2, the two lowest eigenvectors of the $m \times m$ matrix $\chi^T L \chi$ where L is the unnormalized Laplacian of the original graph
- Finally extracting the coordinates as $x^1, x^2 = \chi y^1, \chi y^2$

This method has always been applied with a 100-dimensional HDE, and in the following the two axes within which coordinates x^1, x^2 will be represented will be referred as arbitrary units (AU) and always indicated with a reference to this chapter, so that the reader can easily find out their mathematical meaning if interested.

3.7 Distance metrics between nodes

Also in literature to give meaning to distance between nodes within a graph is often tricky and it strongly depends on what kind of network one is looking at and what nodes and edges actually represent. For this study two measures were considered and briefly explained hereafter.

3.7.1 Shortest path distance

Shortest path distance (or geodesic distance) is the mainly used and accepted distance metric when dealing with graphs. It can be seen as the path connecting two nodes with the minimum cost. This results in two different definitions of shortest path distance, each related to the kind of simple graph that could be both unweighted and weighted. For an unweighted simple graph the cost relates only to the number of edges between the two nodes, while for a weighted simple graph the shortest path is that for which the sum of the weights of its constituents edges is minimized. The distance is then the number of edges or the sum of their weights, respectively. This metric is independent from the layout of the graph because edges connecting nodes are the same regardless of the graph drawing. Its computation belongs to the field of shortest path problems, for which several mathematical methods have been proposed and compared during years [67], but for the purposes of this thesis the intuitive definition given is sufficient.

3.7.2 Euclidean distance

Euclidean distance is one of the most widely used distance metrics outside the world of graph theory. Indeed it requires that points between which to calculate the distance have assigned coordinates. It has been said that not always in graph theory nodes are drawn with meaningful coordinates, so this metric that strongly depends on the layout is often discarded. In the case of this study the graph layout is constructed through the eigen-projection in HDE subspace method, which leads the nodes coordinates to be meaningful. They do not actually have a physical meaning, but the two dimensions expressed in arbitrary units used for the drawing relates to some special matrices as seen in 3.6. For these reasons the decision to use the Euclidean distance was made in order to have a measure which depends on the used graph layout, as opposed to the shortest path distance.

For the 2D case the mathematical definition of Euclidean distance between the points p and q having coordinates (p_1, p_2) and (q_1, q_2) respectively, is:

$$d_E(p, q) = \sqrt{(q_1 - p_1)^2 + (q_2 - p_2)^2} \quad (15)$$

4 Applications and results

The applications of the mathematical methods and the corresponding results will be divided in two sections. The first one will focus on spatial organization and neural assemblies which can be found applying spectral clustering on neurons. The second one will aim to investigate on temporal organization and network development and changes switching between ongoing and odour stimulated activity.

4.1 Spatial organization and neural assemblies

Neural assemblies are groups of neurons which activate synchronously, and they are a very interesting aspect of functional connectivity. Clustering algorithms are a natural tool for assessing them starting from neural activity traces recorded with some functional imaging technique. The main reason for the application of spectral clustering is the possible application of the eigengap heuristic method for estimating the optimal number of clusters, which is always a tricky aspect for clustering algorithms.

In particular, in this work spectral clustering is applied to neural fluorescence signals recorded with two-photon excitation microscopy during ongoing activity in zebrafish both in the habenula, a region with relatively few neurons, and in the telencephalon, made up of many more neurons compared to habenula. For the three available fish the number of detected neurons in both habenula and telencephalon is shown in *Table 1*.

Each fish brain region was analysed separately through all the following operations. The habenula of one fish will be taken as example for showing the applied methods, and finally also images obtained for the telencephalon of the same fish will be shown in order to highlight the differences.

	Fish 1	Fish 2	Fish 3
Habenula	696	976	858
Telencephalon	5213	4389	7947

Table 1: Number of detected neurons for habenula and telencephalon of the 3 fish.

4.1.1 Graph construction

From the whole recorded activity only 3.8 minutes (the equivalent of 600 time-samples at a sampling frequency of 2.64 Hz, starting after the first 100 samples) of ongoing activity were isolated, as shown in *Figure 10A* and *10B*, respectively.

Then a similarity graph is constructed with these ongoing signals in which each node represents a neuron and edges are the most significant similarities between neural activations. More precisely $\Delta F/F$ neural signals (the horizontal rows of the matrix shown in *Figure 10B*) are the n data points and the similarity measure between all pairs of points is the Gaussian similarity function (4) computed with $\sigma = 1$ and the correlation distance (2). This distance metric measures the dependence of two vectors, emphasizing the synchronism of the activations. With the similarity matrix obtained so far, the complete k-nearest neighbour similarity graph can be constructed, setting k equal to $\log(n)$. The obtained graph is a weighted, undirected simple graph, and it can be plotted with the two different layouts shown in *Figure 11*. The drawing obtained using the three-dimensional coordinates of the neurons results in a layout that is as physically meaningful as it is confusing (*Figure 11a*), while with the eigen-projection within HDE subspace method the two-dimensional network seems better distributed and the clustering properties of the graph are actually enhanced (*Figure 11b*). The layout of the plotted graph does not affect the implementation of any of the following steps since the graph and its relating matrices remain the same.

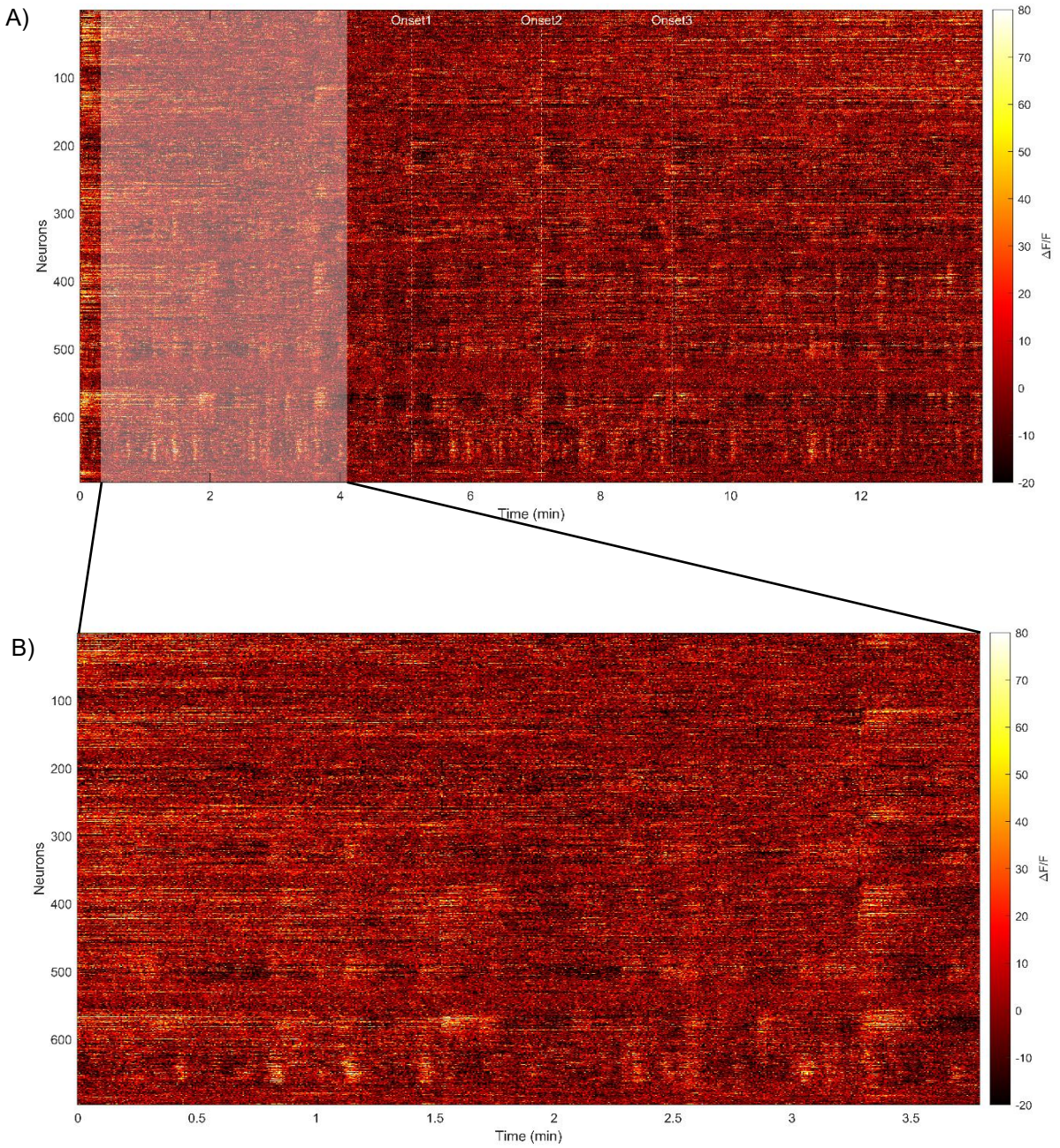

Figure 10: Habenular activity. Fractional change in fluorescence (ΔF/F) signals of the 696 detected neurons. A) Whole 13.8 minutes of recorded activity. The white region contains the selected 3.8 min of ongoing activity, and the dashed white lines indicate the 3 odour onsets. B) Magnification of the 3.8 min of ongoing activity.

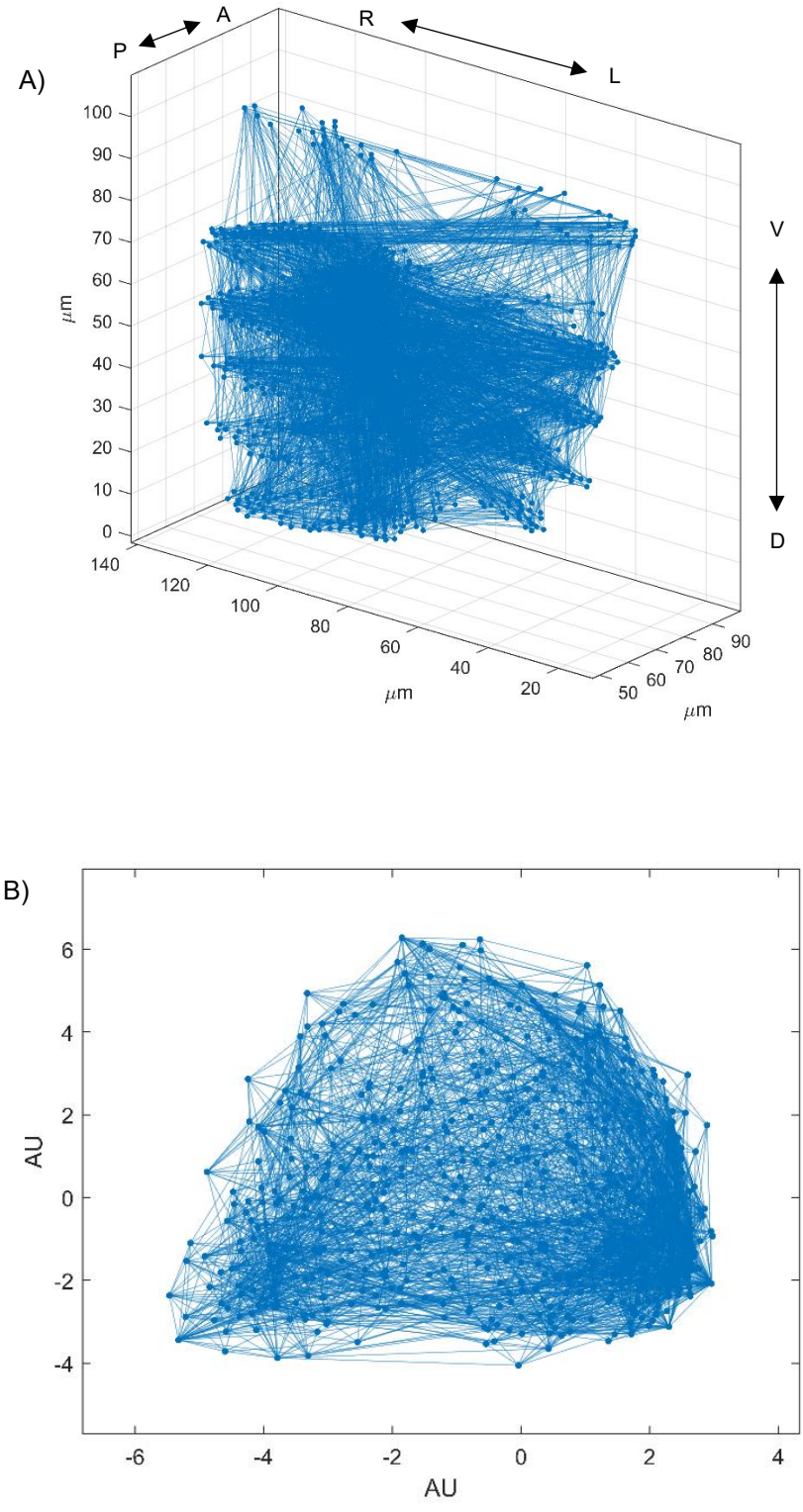

Figure 11: Graph obtained from habenular ongoing activity. Each node represents each of the 696 detected neurons. A) 3D layout obtained with neurons coordinates. Axes are in µm. A: anterior, P: posterior, R: right, L: left, D: dorsal, V: ventral. B) 2D layout obtained with the eigen-projection in HDE subspace method. Axes are in arbitrary units (AU, see 3.6)

4.1.2 Eigengap heuristic method

With the same similarity matrix and the same decisions on how to construct the similarity graph, the eigengap heuristic method can be applied using the random walk normalized Laplacian. In *Figure 12* are shown the ascending distribution of the first 15 eigenvalues (*Figure 12A*) and the differential eigengap computed for the first 14 of them simply subtracting the magnitude of the latter (*Figure 12B*). It always happens that the largest eigengap corresponds to the first eigenvalue, suggesting that this method tends to see all the neurons belonging to the same unique big cluster, which actually means not clustering neurons at all. Therefore, it has been decided to select the predicted optimal number of cluster as the one corresponding to the second largest eigengap. For example, for the case shown in *Figure 12B* the optimal number of clusters is equal to 2.

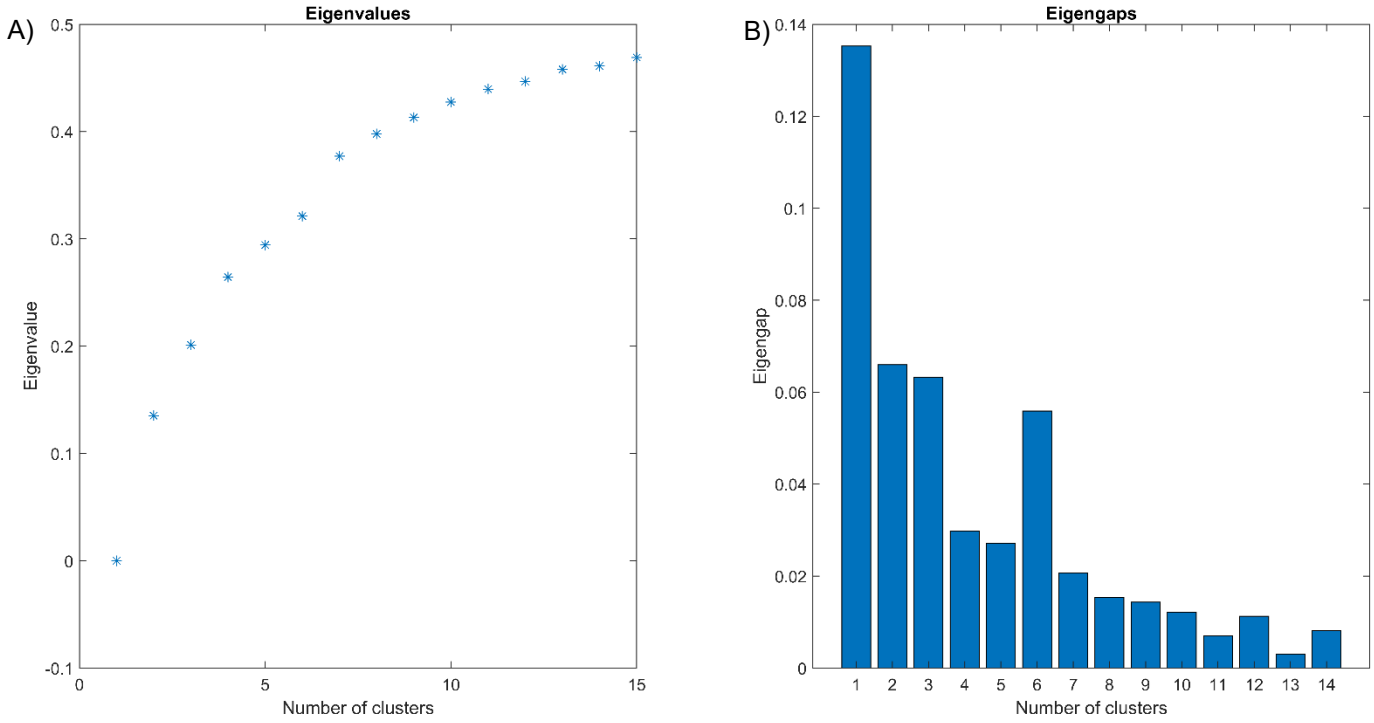

Figure 12: Eigengap heuristic method applied on graph obtained from habenular ongoing activity. A) Distribution of the first 15 eigenvalues of the random walk normalized Laplacian. B) Bar plot of the eigengaps of the first 14 eigenvalues, computed subtracting the magnitude of the later eigenvalue from each of the first 14 eigenvalues. The optimal number of clusters is chosen as the eigenvalue corresponding to the second larger eigengap (a number of clusters equal to 1 is always discarded).

4.1.3 Spectral clustering

With the fixed optimal number of clusters the random walk normalized spectral clustering algorithm can be run, again with the same similarity matrix and the same decisions on how to construct the similarity graph. The results of the clustering algorithm are shown in *Figure 13* and *Figure 14*. The clustered graph (*Figure 13*) plotted with the eigen-projection in HDE subspace method shows clearly separate clusters, which can be visualized also in the 3D physical representation of the neurons as in *Figure 14A*. In *Figure 14B* are shown the neural fluorescence traces of the neurons belonging to the two detected clusters.

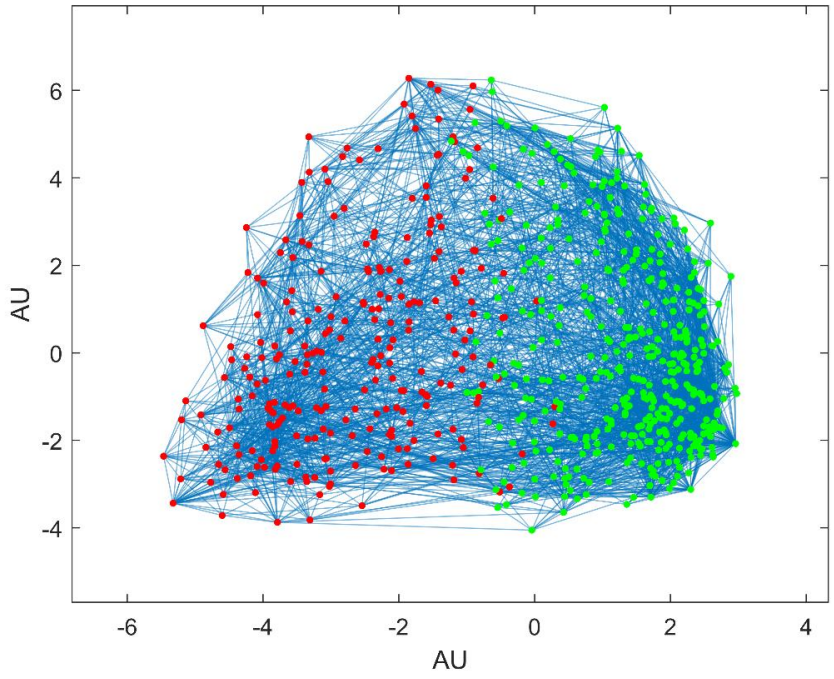

Figure 13: Spectral clustering algorithm applied on the graph obtained from habenular ongoing activity. Each node represents each of the 696 detected neurons. Nodes are coloured based on the belonging cluster (red cluster: 436 neurons, green cluster: 260 neurons). 2D layout obtained with the eigen-projection in HDE subspace method. Axes are in arbitrary units (AU, see 3.6).

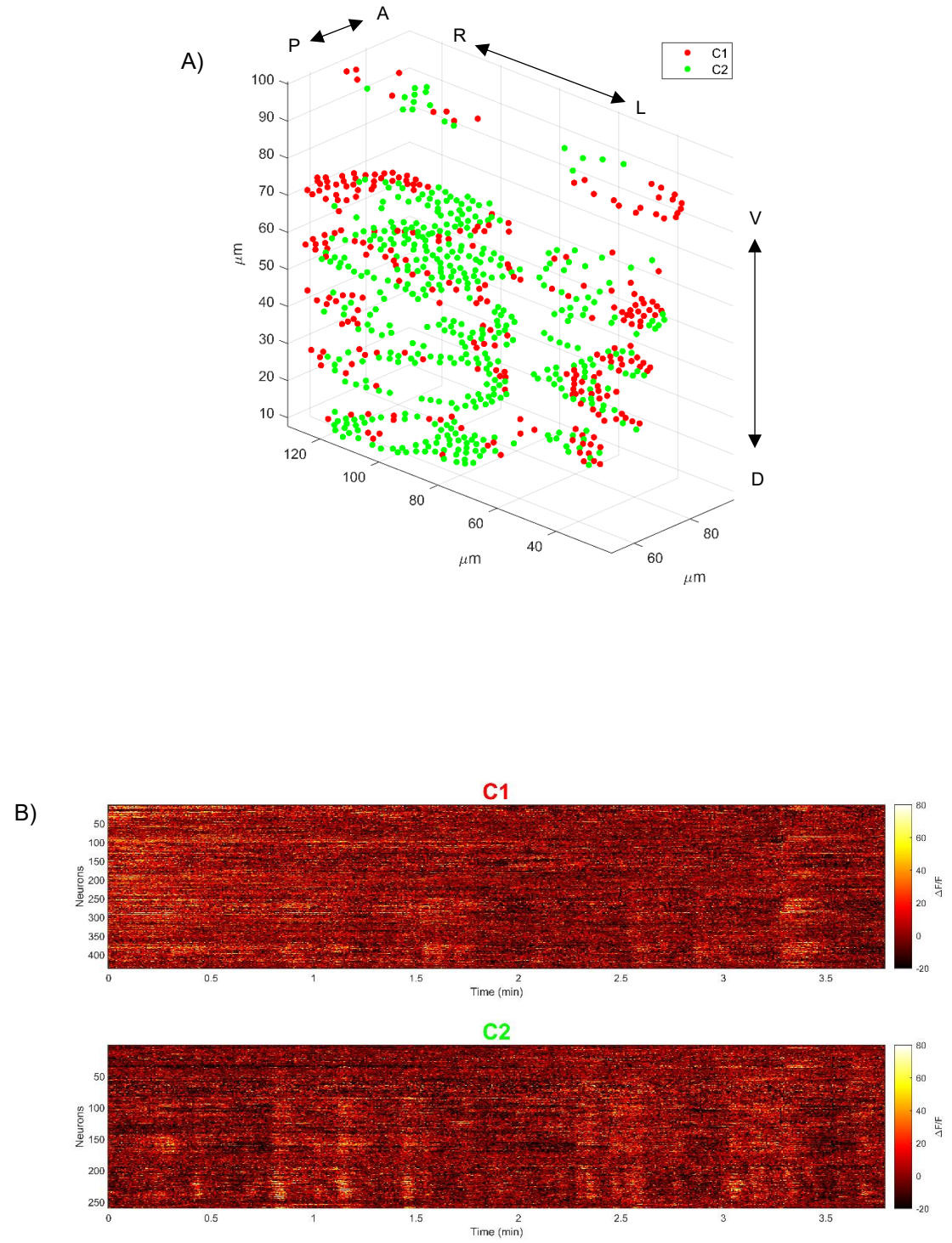

Figure 14: Spectral clustering algorithm results on neurons and fractional change in fluorescence (ΔF/F) signals. A) Clustered neurons coloured based on the belonging cluster. Axes are in μm. A: anterior, P: posterior, R: right, L: left, D: dorsal, V: ventral. B) Clustered fractional change in fluorescence (ΔF/F) signals of the 3.8 min of ongoing activity. Red cluster C1: 436 neurons, Green cluster C2: 260 neurons

4.1.4 Overall results

As mentioned before, in the following pages (*Figure 15 – Figure 19*) are shown all the steps for one fish telencephalon. The main structural difference is the number of detected neurons and so the number of nodes in the graph, which is substantially larger in this case. This results in a visualization issue when looking at the graph, because nodes are not always well separated and often edges overlap making the drawing not very clear. However, the graphs are shown in order to allow a full comparison between habenula and telencephalon.

Overall, for both brain regions of all fish the predicted number of clusters is shown in *Table 2*.

	Fish 1	Fish 2	Fish 3
Habenula	2	3	5
Telencephalon	3	5	4

Table 2: Number of clusters predicted with the eigengap heuristic method for habenula and telencephalon of the 3 fish.

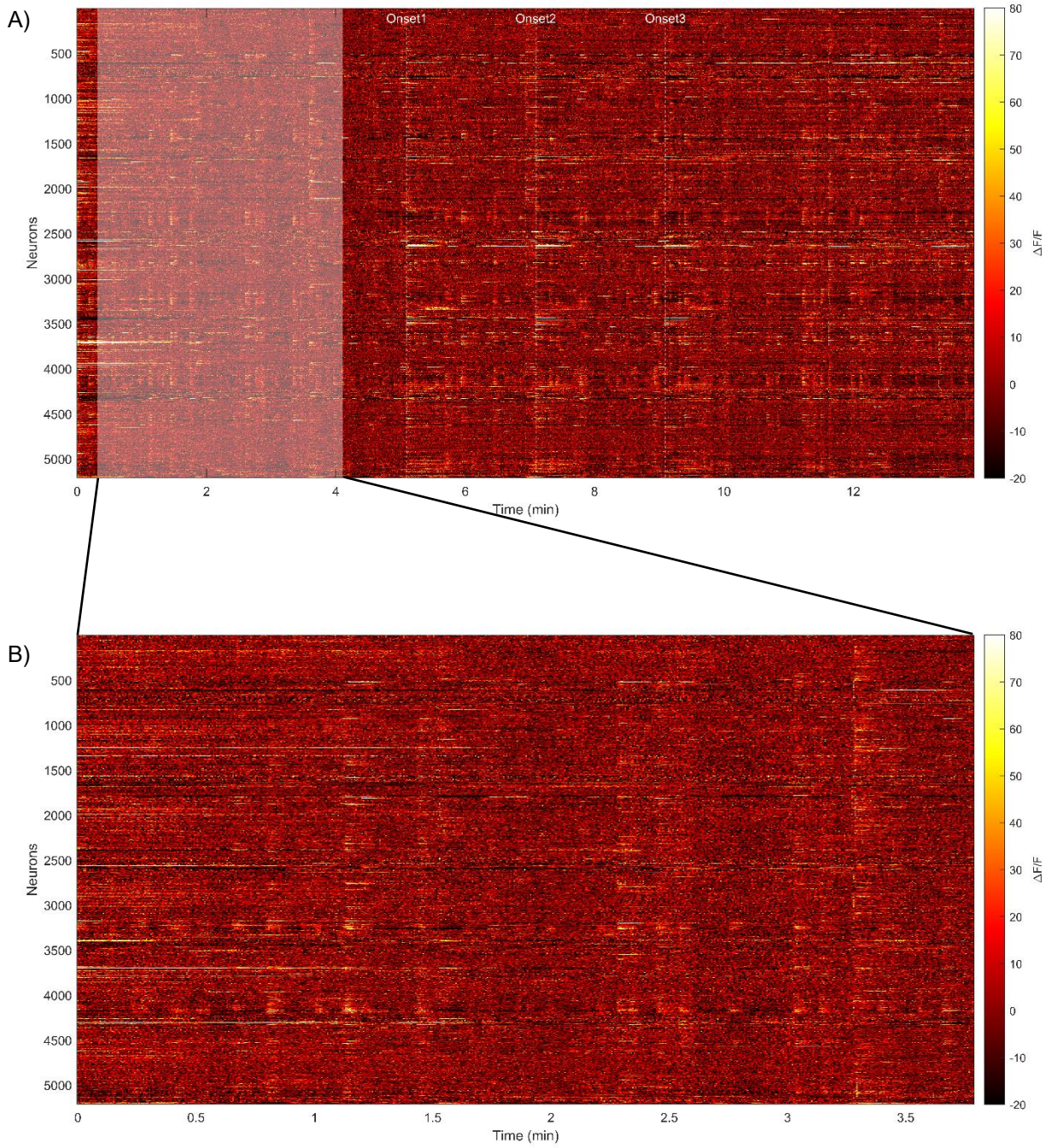

Figure 15: Telencephalon activity. Fractional change in fluorescence (ΔF/F) signals of the 5213 detected neurons. A) Whole 13.8 minutes of recorded activity. The white region contains the selected 3.8 min of ongoing activity, and the dashed white lines indicate the 3 odour onsets. B) Magnification of the 3.8 min of ongoing activity.

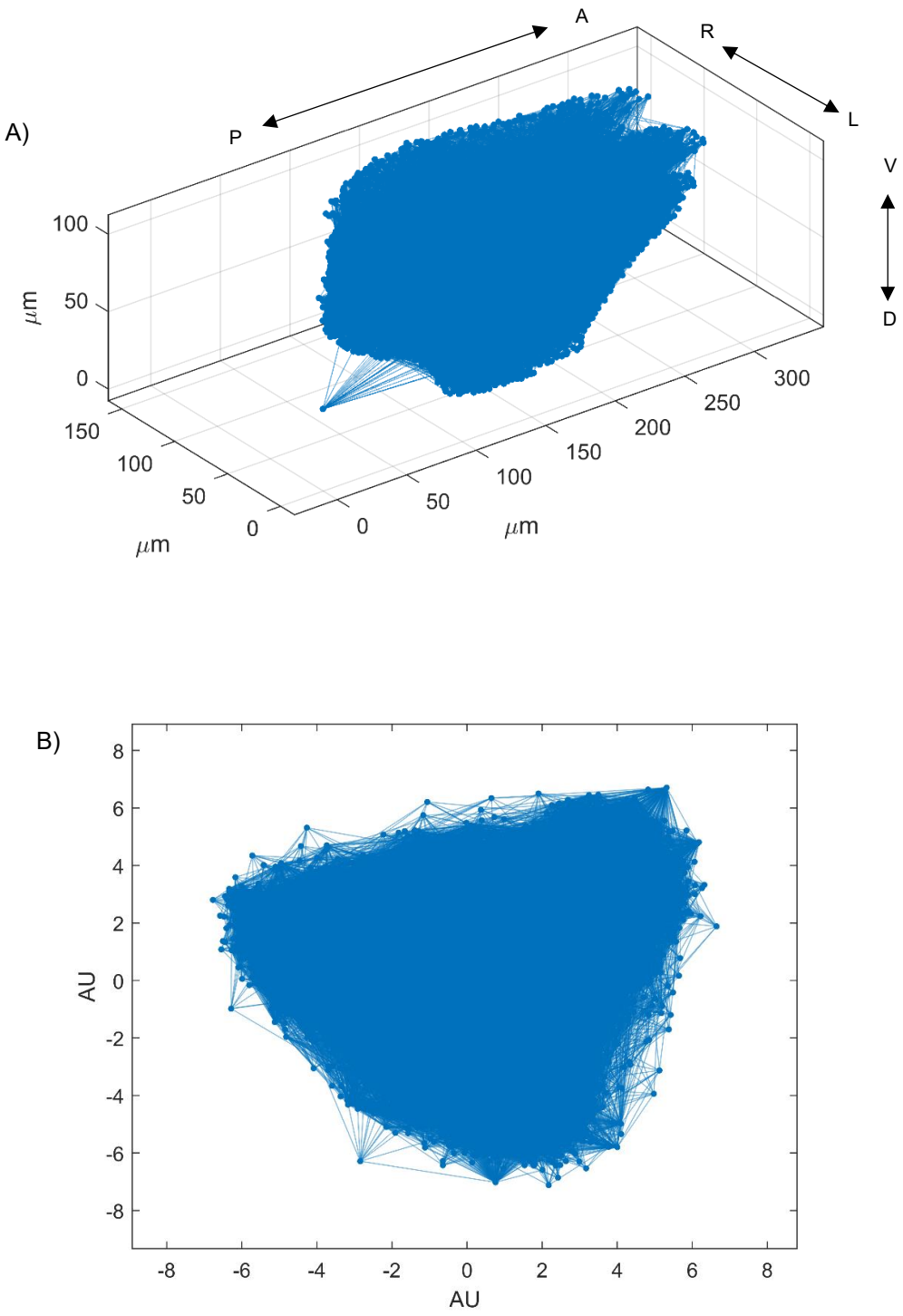

Figure 16: Graph obtained from telencephalon ongoing activity. Each node represents each of the 5213 detected neurons.

A) 3D layout obtained with neurons coordinates. Axes are in μm. A: anterior, P: posterior, R: right, L: left, D: dorsal, V: ventral. B) 2D layout obtained with the eigen-projection in HDE subspace method. Axes are in arbitrary units (AU, see 3.6)

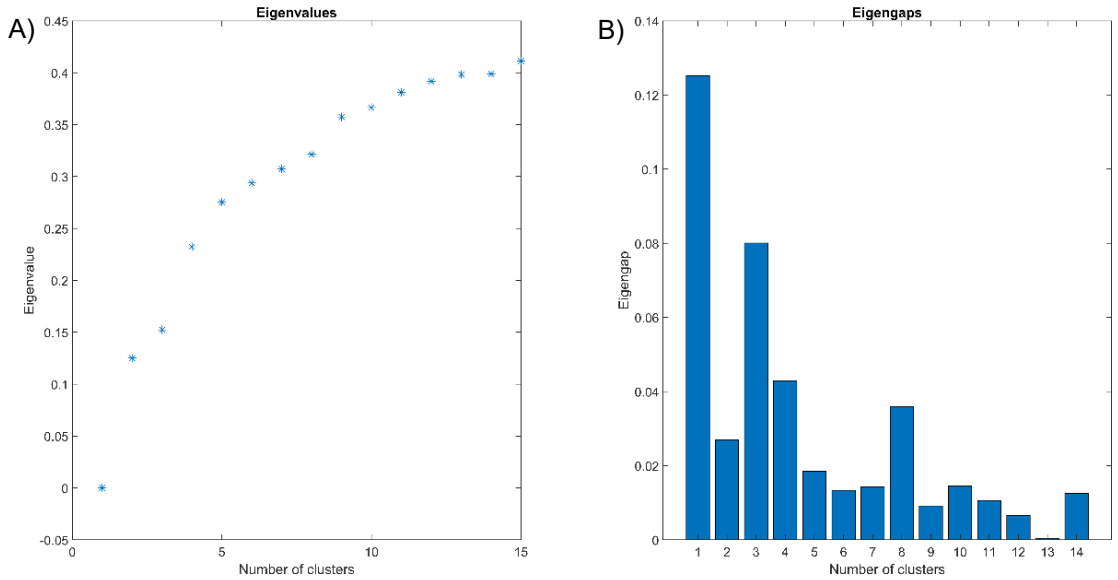

Figure 17: Eigengap heuristic method applied on graph obtained from telencephalon ongoing activity.
A) Distribution of the first 15 eigenvalues of the random walk normalized Laplacian. B) Bar plot of the eigengaps of the first 14 eigenvalues, computed subtracting the magnitude of the later eigenvalue from each of the first 14 eigenvalues. The optimal number of clusters is chosen as the eigenvalue corresponding to the second larger eigengap (a number of clusters equal to 1 is always discarded).

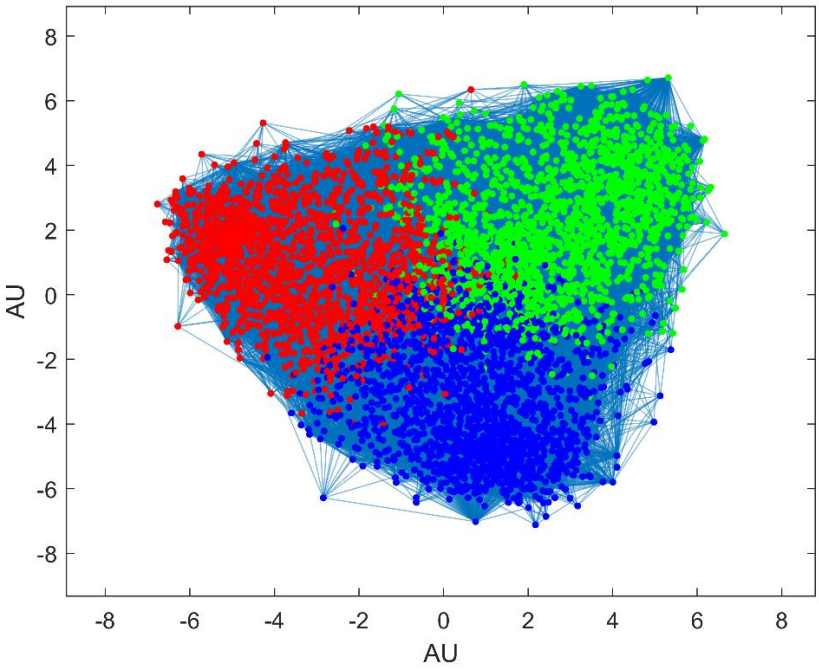

Figure 18: Spectral clustering algorithm applied on the graph obtained from telencephalon ongoing activity. Each node represents each of the 5213 detected neurons. Nodes are coloured based on the belonging cluster (red cluster: 1765 neurons, green cluster: 1767 neurons, blue cluster: 1681 neurons). 2D layout obtained with the eigen-projection in HDE subspace method. Axes are in arbitrary units (AU, see 3.6)

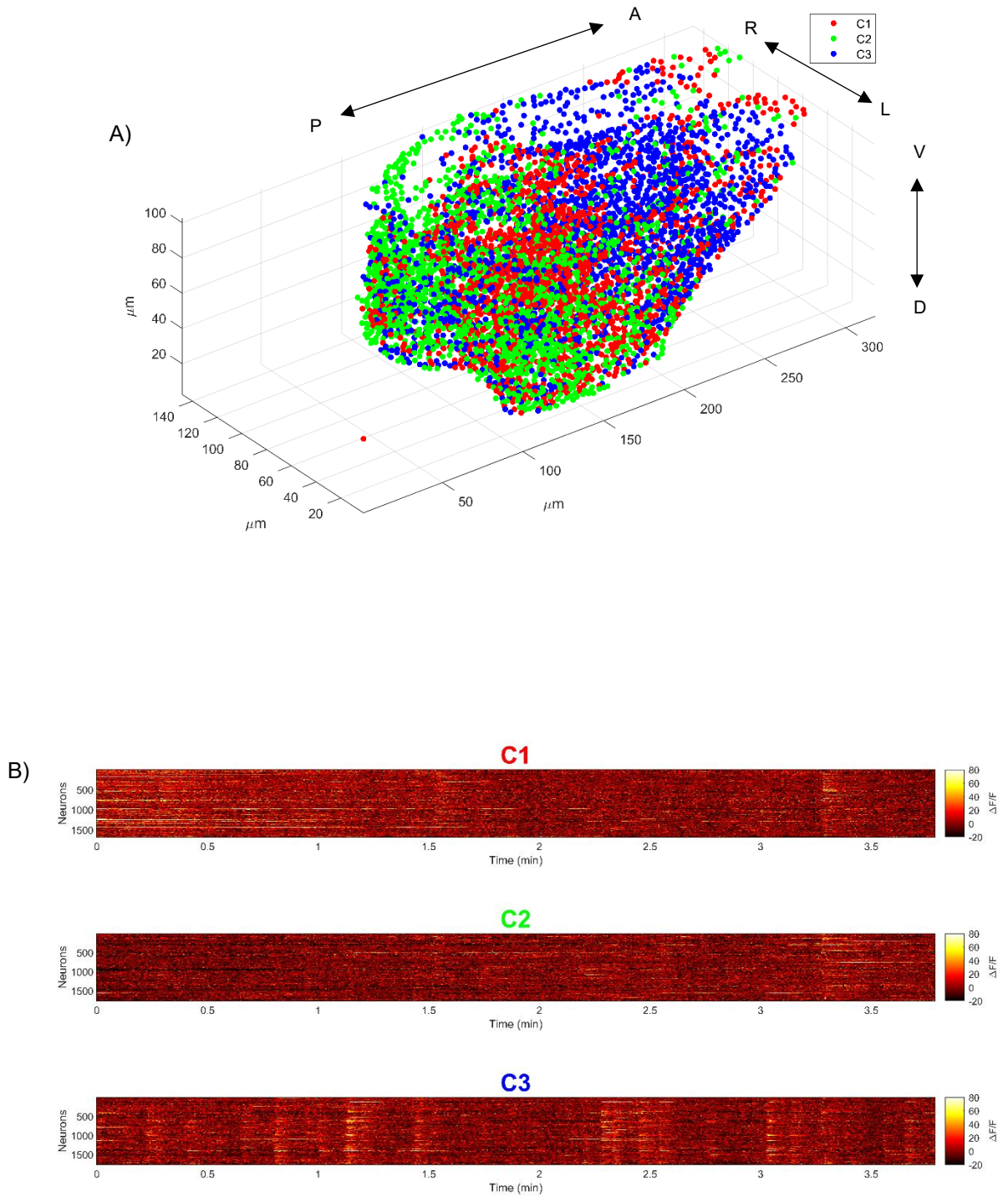

Figure 19: Spectral clustering algorithm results on neurons and fractional change in fluorescence (ΔF/F) signals. A) Clustered neurons coloured based on the belonging cluster. Axes are in μm. A: anterior, P: posterior, R: right, L: left, D: dorsal, V: ventral. B) Clustered fractional change in fluorescence (ΔF/F) signals of the 3.8 min of ongoing activity. Red cluster C1: 1765 neurons, Green cluster C2: 1767 neurons, Blue cluster C3: 1681 neurons

4.2 Temporal organization and network development

This second objective focuses on temporal development of the network, trying to assess the diversity of the types of neural activation during ongoing activity and odour stimulated activity. In order to evaluate temporal organization a change of prospective is needed. The main idea of looking at a graph made up of frames of coactive neurons, the so called activity patterns, is taken from the brilliant work of Avitan *et al.* [17]. Then the analytical methodologies for computing distances between nodes are specifically thought for the kind of investigations interesting and useful for the purposes of the lab.

Each fish brain region was analysed separately throughout the following operations, which are shown using images obtained from one example fish telencephalon. As before, also images referring to the same steps for habenula are presented for comparison. Then the computed distances are examined together along fish, for telencephalon and habenula separately, in order to find a common trend.

4.2.1 Binarization and activity patterns

As before, the starting dataset is the neural activation matrix containing $\Delta F/F$ signals (*Figure 20A*). A common operation performed in literature on this kind of matrix is to binarize it by isolating calcium events. As in [17] an event is detected for each neuron when $\Delta F/F$ signal exceeds two standard deviations above the mean. The resulting binarized matrix contains 1 in those frames recognized as events and 0 otherwise (*Figure 20B*). Only those frames with a relatively high number of coactive neurons are isolated. The threshold for the number of coactive neurons is selected by the following steps: first the binarized activity matrix is randomly shuffled 500 times along neurons, keeping the number of events per cell identical but changing their timing, then the threshold is set equal to the 95^{th} percentile of the number of coactive neurons (at single frame resolution) within this shuffled dataset. These active frames are visually depicted as the "blackest columns" in *Figure 20B*, and they bring two different information: obviously they represent time samples in which neurons are more active and they allow a time tracking of the neural activation, but they also represent patterns of activation along neurons thanks to their neuron-depending entries. For this second reason they are referred to as activity patterns, and this feature is used for constructing the graph.

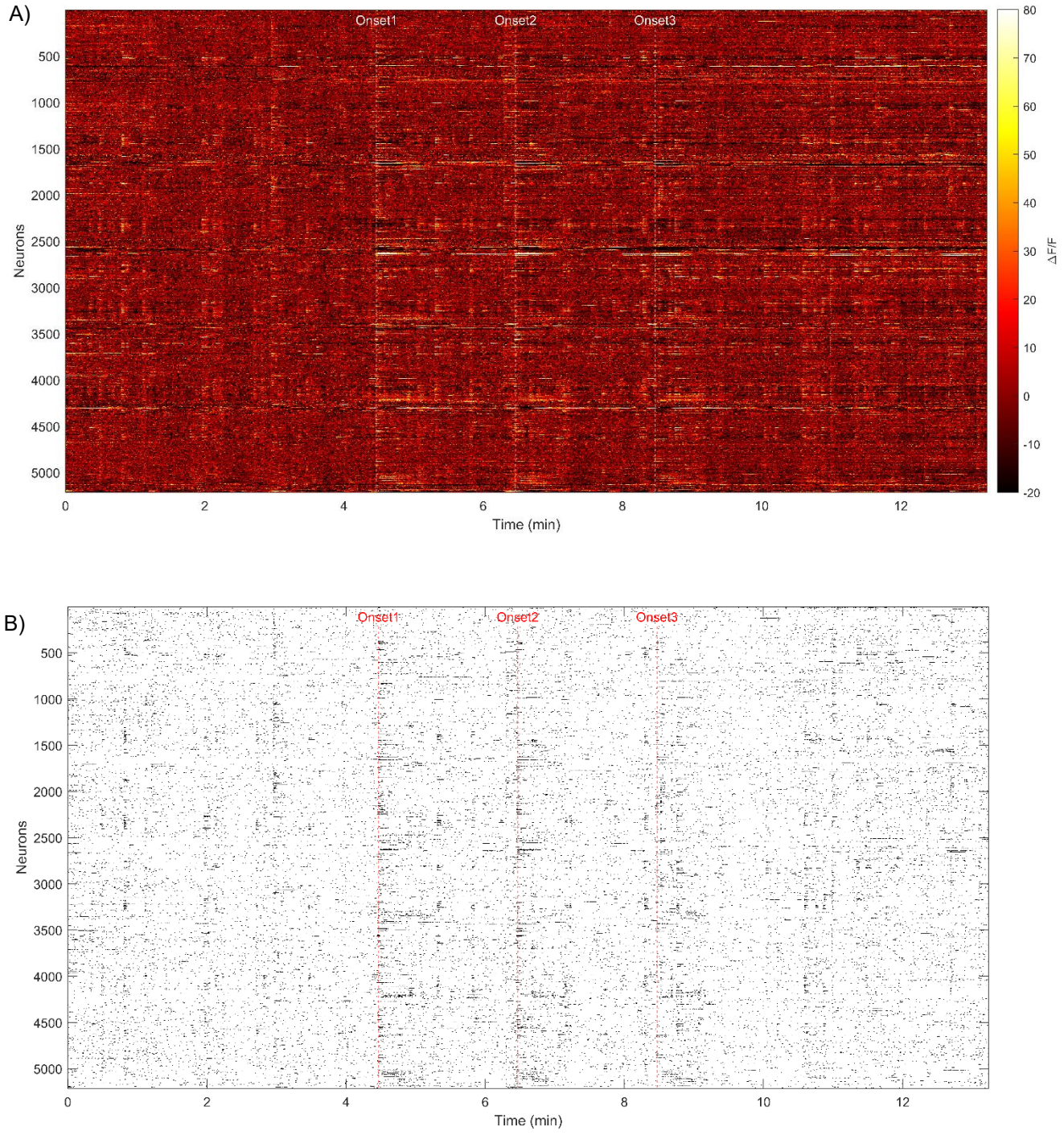

Figure 20: Telencephalon activity and binarized activity. Whole 13.8 minutes of recorded activity of 5213 detected neurons. A) Fractional change in fluorescence ($\Delta F/F$). The dashed white lines indicate the 3 odour onsets. B) Binarized activity. Black: calcium event. The dashed red lines indicate the 3 odour onsets.

4.2.2 Graph construction

With the detected activity patterns a similarity graph is constructed; now the nodes are the activity patterns themselves and cannot be drawn with a geometrical or physical meaning. The Gaussian similarity function (4) with $\sigma = 1$ is again used for computing the similarity measure between all pairs of nodes, but in this case with the cosine distance (3) which is suitable for binary vectors [17]. Once obtained the similarity matrix, the graph is constructed with the k-nearest neighbour method (k equal to $\log(n)$) and results in a weighted, undirected simple graph (*Figure 21*). The information about the time tracking is color-coded by the colorbar expressed in minutes, in which the three black lines represent the three odour onsets. The graph is plotted through the eigen-projection in HDE subspace method, that leads to a drawing in which similar activity patterns are close together, and this information will be used when distance between nodes will be analysed. In this case the layout will be partly relevant.

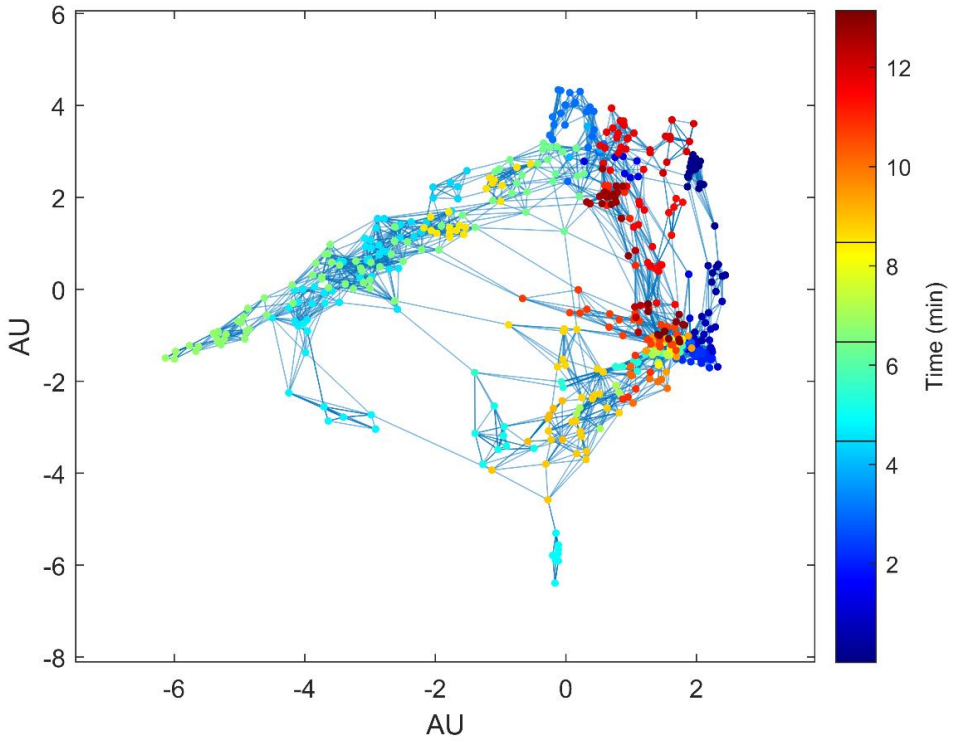

Figure 21: Graph obtained with the activity patterns of telencephalon activity. Each node is one of the 597 detected activity patterns. 2D layout obtained with the eigen-projection in HDE subspace method. Axes are in arbitrary units (AU, see 3.6). Colorbar is in minutes, the three black lines are the three odour onsets (from below: onset 1, onset 2 and onset 3).

4.2.3 Ongoin and odour periods detection

The fish neural network during the experimental procedure is subject to a strong perturbation due to odour stimulation. The aim of this analysis is to visualize how the network behaves in response to that perturbation and whether it changes its internal dynamics comparing pre and post perturbation. In order to track and analyse the state of the network, the activity patterns belonging to three significant periods are selected and shown for the sake of clarity on the binary activity matrix (*Figure 22A*), each of an overall duration of 1.5 minutes:

- Ongoing Pre: one minute and a half of ongoing activity starting after the first 30 seconds of recorded activity (blue panel in *Figure 22A*).
- Odour: the first 30 seconds after each of the three odour onsets (green panels in *Figure 22A*).
- Ongoing Post: one minute and a half of ongoing activity, after the three odour deliveries, starting from the eleventh minute of recorded activity (red panel in *Figure 22A*).

The nodes corresponding to the activity patterns belonging to these three different periods are highlighted with the same colours and shown within the graph in *Figure 22B*.

The choice to select the ongoing activity period both before and after the odour stimulation aims to investigate whether the neural network returns to an ongoing activity similar to the one shown before the stimulation, or the stimulation introduces any significant changes switching back to ongoing activity.

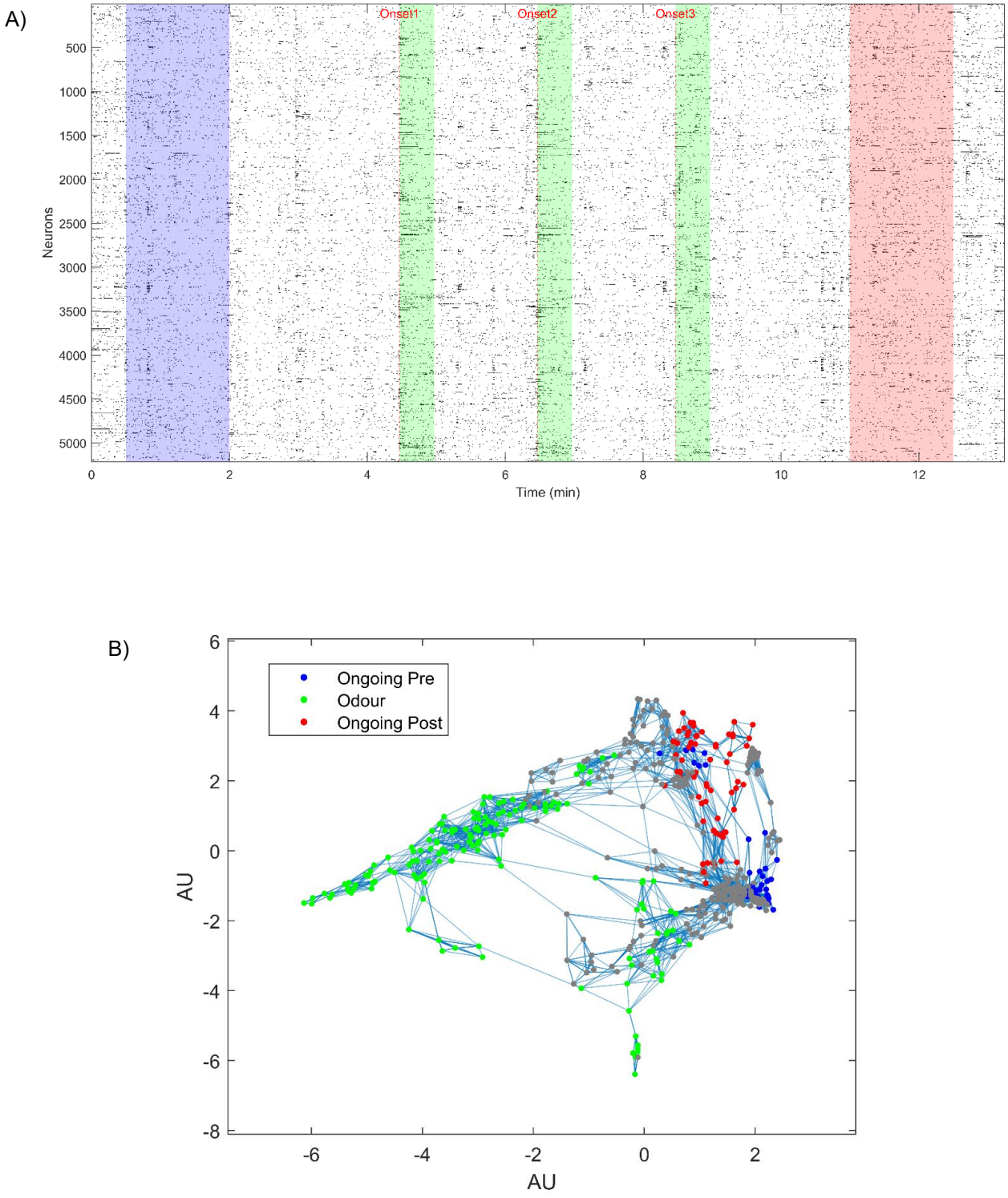

Figure 22: Telencephalon periods detection. A) Binarized activity. The dashed red lines indicate the 3 odour onsets and the coloured panels the three periods. B) Graph obtained with the activity patterns of telencephalon activity. Each node is one of the 597 detected activity patterns. 2D layout obtained with the eigen-projection in HDE subspace method. Axes are in arbitrary units (AU, see 3.6). Nodes are highlighted with the same colour code indicated in the legend. (blue: ongoing pre, green: odour, red: ongoing post)

4.2.4 Distance assessments

Once activity patterns belonging to different behavioural states have been identified, a way for quantifying similarities and differences between them is to analyse the distribution of nodes both intra and inter periods. This can ultimately lead to a comparison of network activity states and their alterations both in a single fish and across animals. Indeed, sparsity within the graph means that activity patterns differ from each other in terms of diversity of active neurons, while close nodes reflect similar activity patterns. For each brain region of each animal on the graph which highlights activity patterns belonging to the three different periods (*Figure 22* for the example animal) two distance measures (Euclidean and shortest path distance) are computed both between nodes belonging to the same period, to assess the intra period sparsity, and between nodes belonging to different periods, for evaluating the inter periods differences. Shortest path distance is independent from the graph layout and it relates to the sum of the edges connecting two nodes. Euclidean distance (15) is indeed computed starting from the nodes coordinates obtained with the eigen-projection method in HDE subspace method, and so strongly layout-dependent. Both the distances are computed as:

- pairwise distance between nodes belonging to the same periods (indicated as "same period" in the following figures)
- pairwise distance between nodes belonging to one period versus nodes belonging to another one (indicated as "different periods" in the following figures)

Then both the distances are normalized with respect to the maximum distance (Euclidean or shortest path, respectively) within the graph, so that the comparison across fish is allowed. Finally distances are plotted with a violin plot [68], an easy-to-read substitute of a box plot that adds information about the distribution of the data, in which the density trace is plotted symmetrically to the left and the right of the vertical box plot

In *Figure 23* are shown the four plots obtained from the graph from *Figure 22*. On the left (*Figure 23A* and *23B*) are shown the two plots of Euclidean and shortest path distances between points within the same period, with the same colour code used before (blue: ongoing pre, green: odour, red: ongoing post). On the right (*Figure 23C* and *23D*)

there are the plots for the inter periods case, in which colours are chosen based on the comparison they represent (green water: ongoing pre versus odour, purple: ongoing pre versus ongoing post, light brown: odour versus ongoing post).

The typical wavelike shape of the two shortest path plots on the bottom (*Figure 23B* and *23D*) is due to the fact that, by construction, the edges of the graph have unlikely light weights, so the summation of each edge adds a relatively large value to the path, resulting in this uneven distribution.

Wilcoxon ranksum test was used for paired comparisons for testing the hypothesis of equal median and p values are indicated in the caption of the figure as: * $p<0.05$, ** $p<0.01$, *** $p<0.001$.

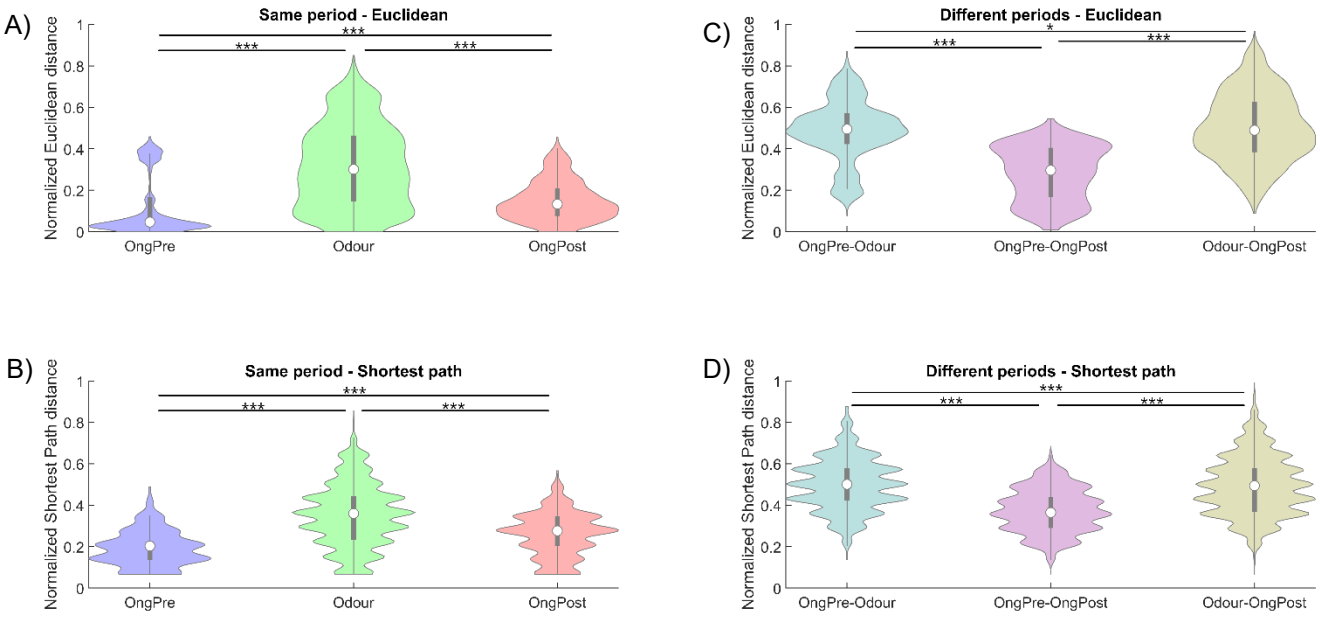

*Figure 23: Violin plots of the intra and inter periods distances for telencephalon activity of the example fish. A) Euclidean distance between nodes belonging to the same period. B) Shortest path distance between nodes belonging to the same period. C) Euclidean distance between nodes belonging to different periods. D) Shortest path distance between nodes belonging to different periods. Colour code: blue: intra ongoing pre, green: intra odour, red: intra ongoing post, green water: inter ongoing pre versus odour, purple: inter ongoing pre versus ongoing post, light brown: inter odour versus ongoing post. Violin plot: white circle: median, end of the thick grey line: 25th (bottom) and 75th (top) percentiles, end of the thin grey line: lower (bottom) and upper (top) adjacent values not considered outliers. Wilcoxon ranksum test: * $p<0.05$, *** $p<0.001$*

4.2.5 Overall results

In the following (*Figure 24 – Figure 27*) the same results for the habenula of the same example fish are presented.

The normalization of the distances with respect to the maximum for each fish brain region allow the comparison across fish. For this purpose, for telencephalon and habenula respectively, Euclidean and shortest path distances computed for the three available fish are grouped and plotted together keeping the intra and inter period meaningful partitions. This procedure leads to the overall plots shown for the telencephalon in *Figure 28* and for the habenula in *Figure 29*.

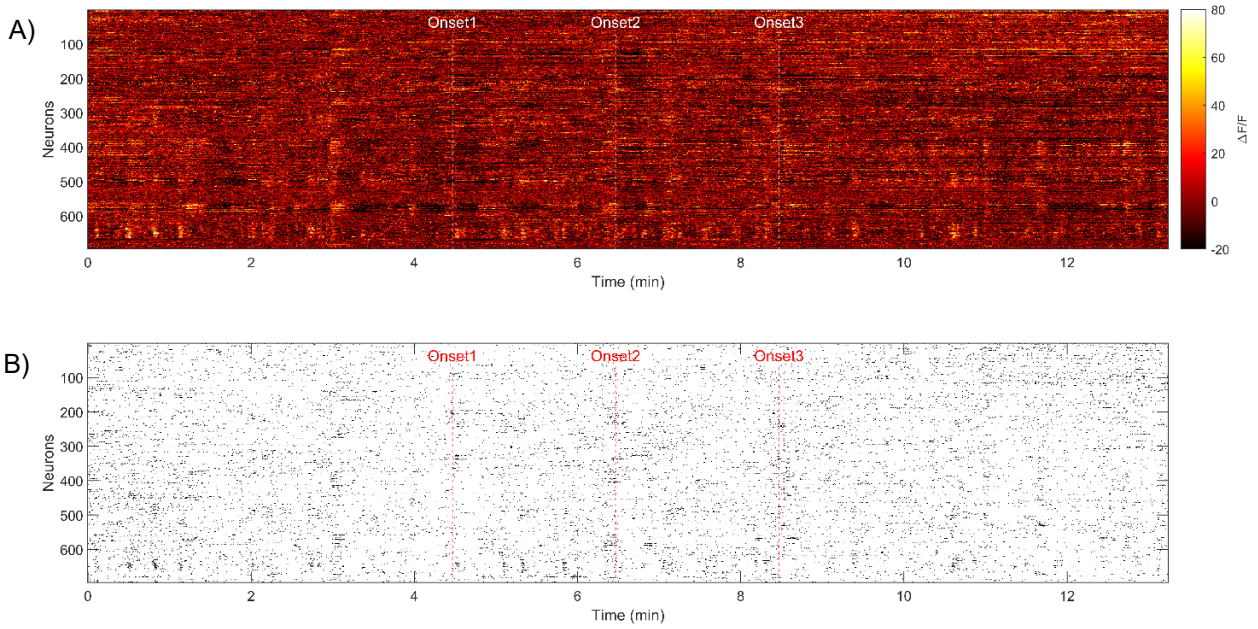

Figure 24: Habenular activity and binarized activity. Whole 13.8 minutes of recorded activity of 696 detected neurons. A) Fractional change in fluorescence ($\Delta F/F$). The dashed white lines indicate the 3 odour onsets. B) Binarized activity. Black: calcium event. The dashed red lines indicate the 3 odour onsets.

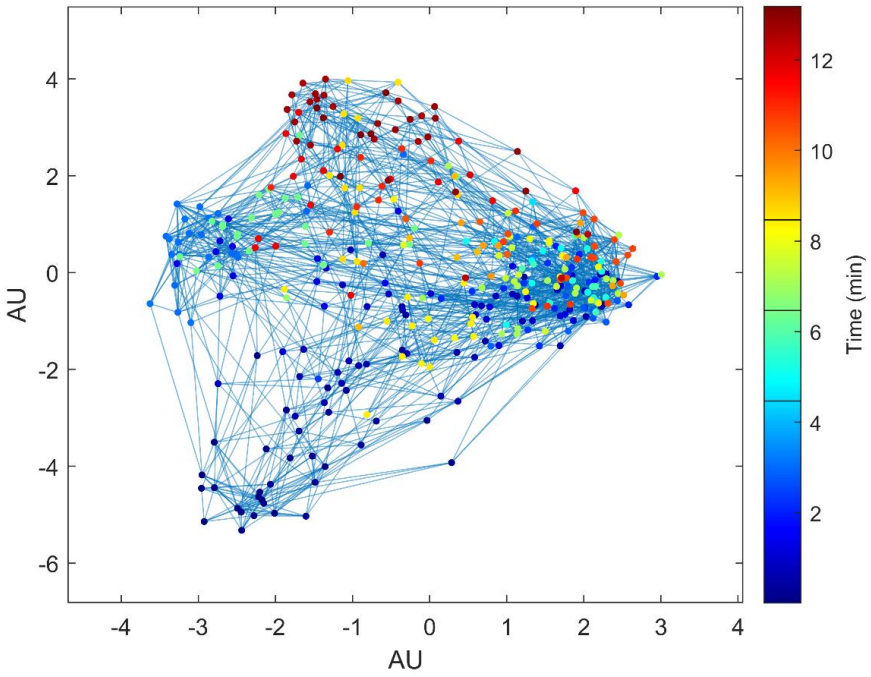

Figure 25: Graph obtained with the activity patterns of habenular activity. Each node is one of the 371 detected activity patterns. 2D layout obtained with the eigen-projection in HDE subspace method. Axes are in arbitrary units (AU, see 3.6). Colorbar is in minutes, the three black lines are the three odour onsets (from below: onset 1, onset 2 and onset 3).

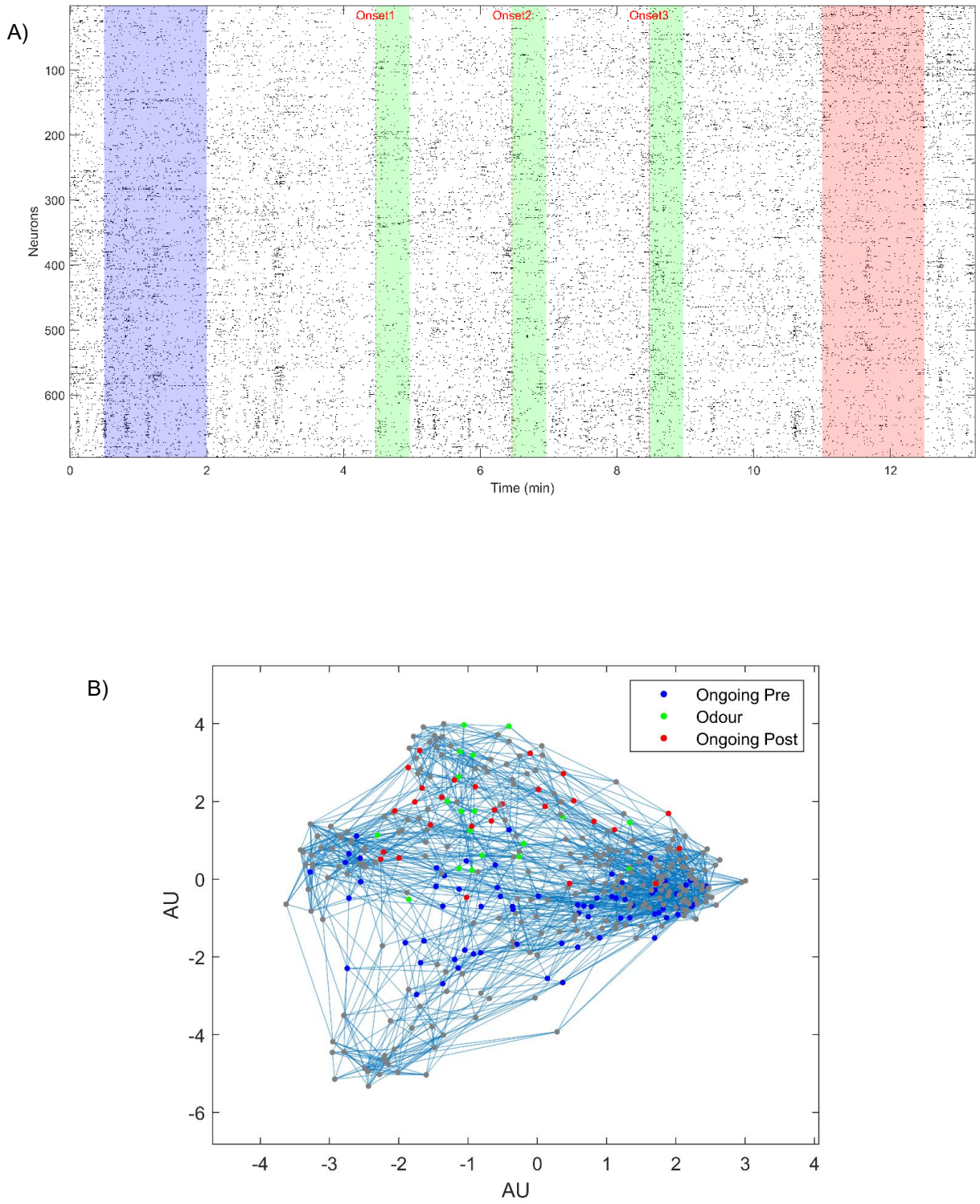

Figure 26: Habenular periods detection. A) Binarized activity. The dashed red lines indicate the 3 odour onsets and the coloured panels the three periods. B) Graph obtained with the activity patterns of habenular activity. Each node is one of the 371 detected activity patterns. 2D layout obtained with the eigen-projection in HDE subspace method. Axes are in arbitrary units (AU, see 3.6). Nodes are highlighted with the same colour code indicated in the legend. (blue: ongoing pre, green: odour, red: ongoing post)

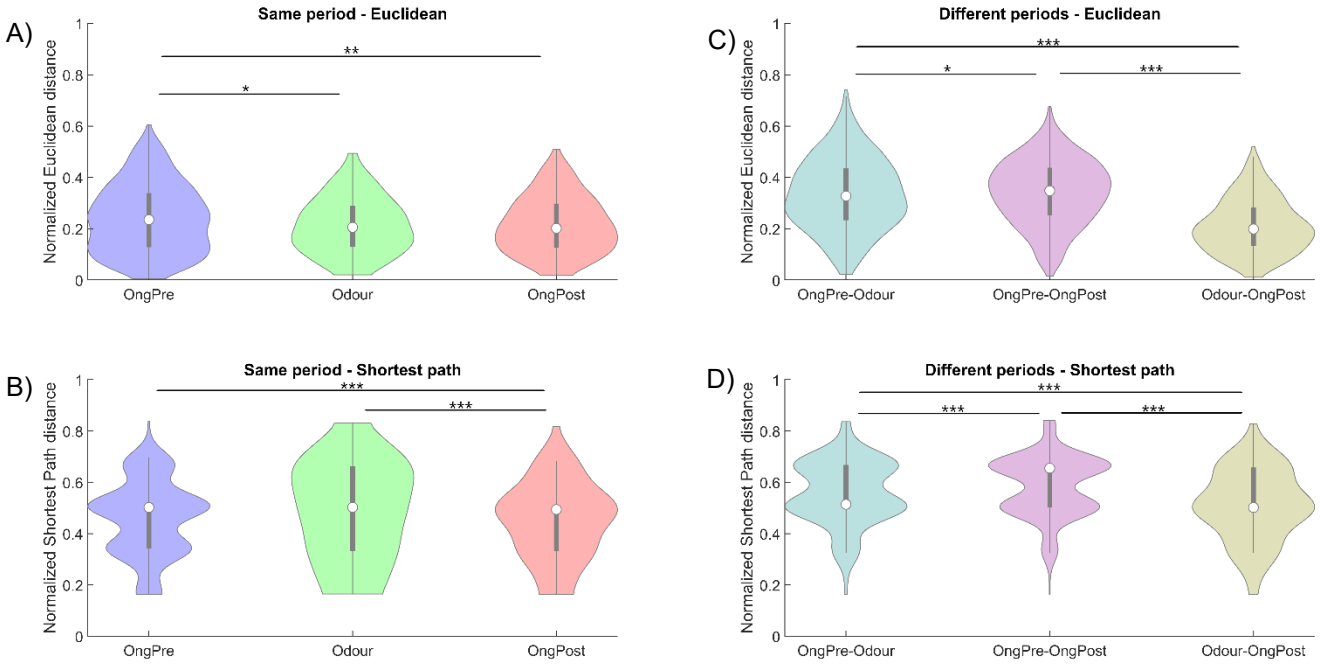

*Figure 27: Violin plots of the intra and inter periods distances for habenular activity of the example fish. A) Euclidean distance between nodes belonging to the same period. B) Shortest path distance between nodes belonging to the same period. C) Euclidean distance between nodes belonging to different periods. D) Shortest path distance between nodes belonging to different periods. Colour code: blue: intra ongoing pre, green: intra odour, red: intra ongoing post, green water: inter ongoing pre versus odour, purple: inter ongoing pre versus ongoing post, light brown: inter odour versus ongoing post. Violin plot: white circle: median, end of the thick grey line: 25th (bottom) and 75th (top) percentiles, end of the thin grey line: lower (bottom) and upper (top) adjacent values not considered outliers. Wilcoxon ranksum test: * p<0.05, ** p<0.01, *** p<0.001*

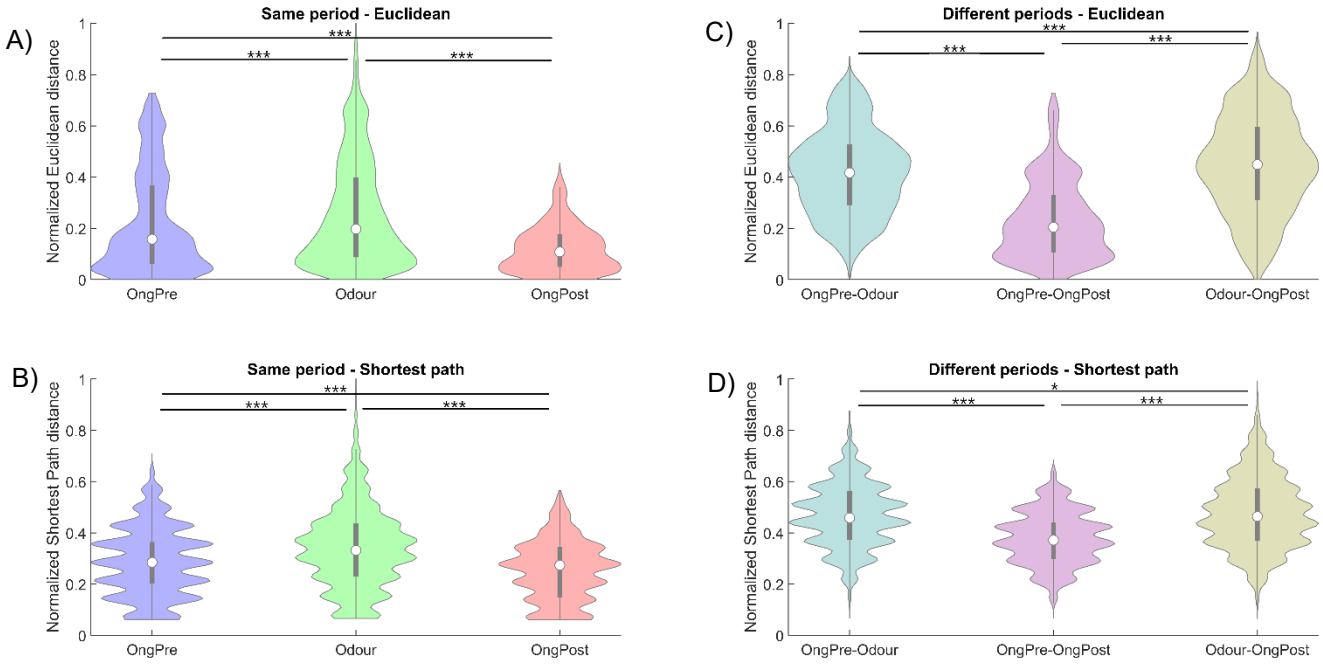

*Figure 28: Violin plots of the intra and inter periods distances for telencephalon activity of the three fish. A) Euclidean distance between nodes belonging to the same period. B) Shortest path distance between nodes belonging to the same period. C) Euclidean distance between nodes belonging to different periods. D) Shortest path distance between nodes belonging to different periods. Colour code: blue: intra ongoing pre, green: intra odour, red: intra ongoing post, green water: inter ongoing pre versus odour, purple: inter ongoing pre versus ongoing post, light brown: inter odour versus ongoing post. Violin plot: white circle: median, end of the thick grey line: 25th (bottom) and 75th (top) percentiles, end of the thin grey line: lower (bottom) and upper (top) adjacent values not considered outliers. Wilcoxon ranksum test: * p<0.05, *** p<0.001*

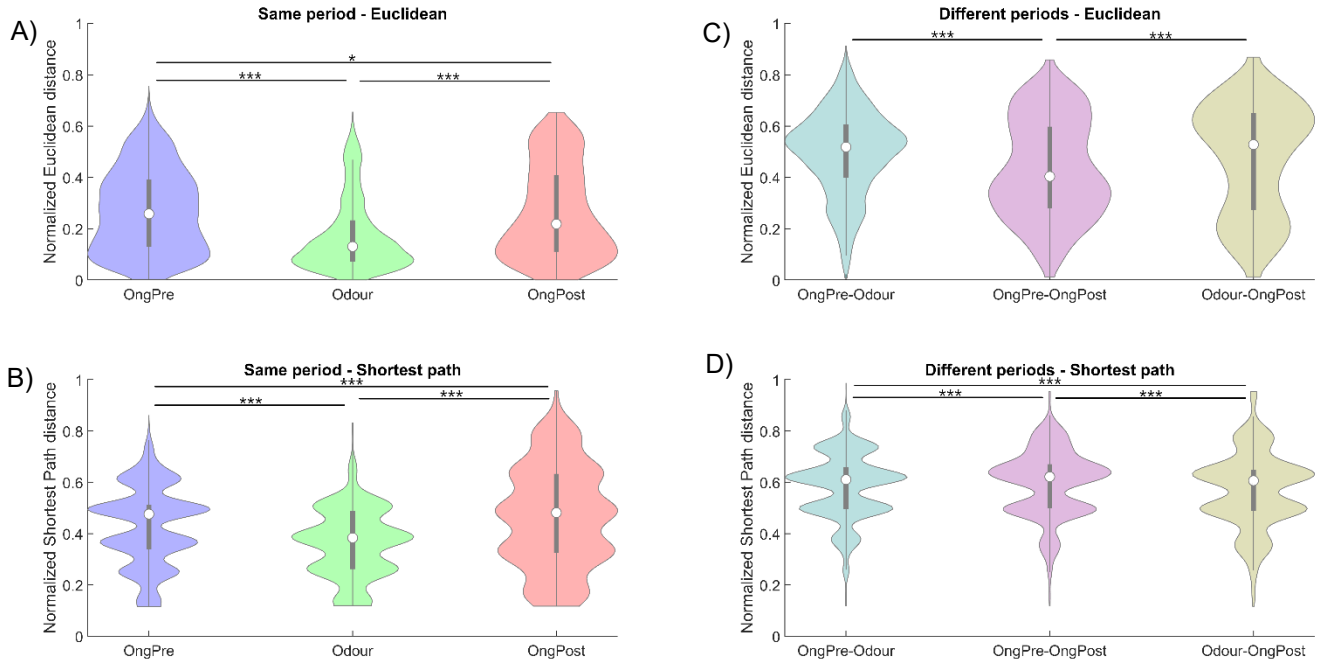

*Figure 29: Violin plots of the intra and inter periods distances for habenular activity of the three fish. A) Euclidean distance between nodes belonging to the same period. B) Shortest path distance between nodes belonging to the same period. C) Euclidean distance between nodes belonging to different periods. D) Shortest path distance between nodes belonging to different periods. Colour code: blue: intra ongoing pre, green: intra odour, red: intra ongoing post, green water: inter ongoing pre versus odour, purple: inter ongoing pre versus ongoing post, light brown: inter odour versus ongoing post. Violin plot: white circle: median, end of the thick grey line: 25th (bottom) and 75th (top) percentiles, end of the thin grey line: lower (bottom) and upper (top) adjacent values not considered outliers. Wilcoxon ranksum test: * p<0.05, *** p<0.001*

5 Discussion

The two performed investigations aim to shed light on two different aspects of functional connectivity. On one hand, the analysis of spatial organization tries to find a helpful method for estimating the number of neural assemblies which synchronously activate during ongoing activity. On the other hand, the investigation about network development focuses on the differences between the neural activity patterns which arise during different cognitive tasks, in the case of this study ongoing activity and odour stimulation.

One of the issues in the lab when dealing with clustering neural activity, especially during ongoing activity, is to predict the optimal number of clusters in which neurons naturally synchronize their activity. Many different methods have been proposed in literature [69][70] and among them in this work the easy-to-use eigengap heuristic method presented by Von Luxburg in [55] is implemented which exploits the properties related to the graph Laplacian. The Laplacian and its spectrum indeed reflect the structure of the graph as the number of connected component is equal to the number of the first null eigenvalues. Also in the case of a graph made up of just one connected component the magnitude of the eigenvalues can suggest the optimal number of clusters in which to divide the graph. In this work all the obtained graphs, both for habenula and telencephalon, are always comprised of a single connected component and the eigengap heuristic method properly applied as in [55] would always predict a single large cluster since the largest eigengap always corresponds to a number of clusters equal to one. For this reason it was decided to disregard the largest eigengap and to choose the final number of clusters as the one corresponding to the second largest eigengap. This slight modification was necessary and seems to suggest that the eigengap heuristic method results in a poor ability to recognize small clusters. Moreover the expected numbers of clusters, both for habenula and telencephalon listed in *Table 2*, have a range between two and five, when five is also the number of clusters selected by Bartoszek and colleagues in [47] for performing k-means on the same habenular fluorescence signals during ongoing activity based on the elbow test. This tendency to underestimate the number of clusters could be due to the high-dimensionality of the data and a sign of high level of overlapping that probably characterizes clusters within their original high-dimensional space. As a matter of fact these conditions could lead to a failure of the eigengap heuristic

method [71]. However, the spectral clustering algorithm was chosen not only for the possibile application of the eigengap heuristic method, but also because it allows the data to be represented in a dimensionality reduced space build through the graph Laplacian. This instead could be a very helpful feature when dealing with this kind of dataset because calcium data are naturally high-dimensional and noisy, and dimensionality reduction tools could be particularly suitable. Besides, clustering time series as $\Delta F/F$ fluorescence traces could be tricky because observations size increases with sampling frequency and sample duration, and the possibility to reduce their dimensions and to visualize them could be preferred.

The analysis on network development over time is a new and complementary approach with respect to the ones already used in the lab, and it reveals interesting results when comparing telencephalon and habenular behaviours. Looking at the graphs obtained with the activity patterns of telencephalon (the one in *Figure 21* and *22B* for the example fish) the network moves within the plot following a precise course: from an initial region where the first detected ongoing activity patterns concentrate, the network tends to travel to new regions in a sparser and often bimodal manner during the stimulation period, and it finally returns to the starting ongoing area. This clear trend is strongly followed by all telencephalon networks, but it is not visible for the habenular ones. For the latter (graph shown in *Figure 25* and *26B* for the example fish), it is more difficult to identify precise regions in which the similar activity patterns are concentrated, and it also occurs that activity patterns belonging to periods of ongoing activity pre and post stimulation are quite distant from each other within the plot. These different behaviours suggest on one hand that habenula presents a more varied activity also at a short time scale during a single cognitive task with respect to telencephalon, and on the other hand that telencephalon circuits are much more plastic than the habenular ones and capable to reorganize even after the perturbation occurs.

These results could be better analysed and quantified looking at the violin plots of the computed distances. Starting from telencephalon (example fish in *Figure 23* and three fish overall in *Figure 28*) both the two intra-period distances show that lengths within the odour period are larger than those within ongoing periods, pointing out the diversity and multi-modality typical of the activity patterns of the telencephalon. The inter-periods

distances are significantly lower when computed between ongoing pre and ongoing post periods with respect to both the two ongoing versus odour cases. This quantifies the visual detection of the abovementioned areas in the graph corresponding to ongoing (both pre and post) and odour periods respectively, and can be clues of the synaptic plasticity characteristic of the telencephalon and of the presence of learning behaviours.

On the contrary, the habenula exhibits a different trend. From the plots of the example fish shown in *Figure 27*, it is immediately clear that the intra-period distances follow a different path compared to the telencephalon, and here activity patterns belonging to the odour period are not so well-separated within the drawing. In *Figure 29* the trend observed is that the distance between activity patterns belonging to the odour period are lower than that of the two ongoing periods. Furthermore, the inter-periods distances shown on the right side of the figures reveal less pronounced similarity between the ongoing pre-stimulation period and the ongoing post-stimulation one as compared with the case of telencephalon: the Euclidean distance between ongoing pre and ongoing post periods has a median relative value of 0.4 (with respect to the 0.2 of the same comparison for the telencephalon) and the median of the shortest path distance between the same two periods is even significantly larger than the median of both the comparisons ongoing pre-odour and odour-ongoing post.

Together these data confirm the results of the visual inspection of the graphs meaning that behaviours as network plasticity (that could maybe be ultimately due to synaptic plasticity) and learning after a sensory perturbation are more likely to occur within telencephalon circuits, while the habenula internal state being more affected by odour experience and so less plastic.

5.1 Outlook and future studies

Both aspects of functional connectivity discussed in this thesis are current fields of interest of Yaksi lab and will be probably further investigated in the future. With regards to the analysis on the optimal number of clusters, it could be interesting to apply a technique which looks for the desired number already within a space of reduced dimensionality and not only perform the clustering in the new space. The dimensionality reduction tool could be one of many available ones in literature such as the principal

components analysis (PCA), t-distributed stochastic neighbour embedding (t-SNE), uniform manifold approximation and projection (UMAP) or some machine learning and deep learning algorithms. Regarding the study of network development, a first computational idea to improve the performance of the detection of activity patterns could affect the denoising and the binarization process of the $\Delta F/F$ signals. For this purpose a deconvolution method was proposed by Friedric *et al.* [72] tailor-made for traces of whole-brain larval zebrafish and this advanced method of calcium events extraction could help for binarizing the neural signals and so detecting the activity patterns. A further implementation could be to look at the periods of ongoing activity between the odour stimulations which can be very interesting to analyse more in depth the plasticity and the learning behaviour of the neural circuits also at a short time scale, meaning that the animal during that period is no longer subjected to the stimulation, but has not yet had time to fully relax. Ultimately, there is the possibility to combine the two approaches of constructing the graph which represents activity patterns and network development and performing on it spectral clustering as in [17]. This leads to a new way to see neural assemblies because one neuron can belong to more than one cluster and therefore hub neurons could be identified, but for the application of this method some parameters need to be optimized and this could be a tricky operation.

Lastly, all the graph-based algorithms used in this work do not depend on the type of brain region analysed or on the type of sensor stimulation performed because they only require fractional change in fluorescence signals easily obtained in the lab, so it could be interesting to apply them on data acquired on other parts of the fish brain and during diverse behavioural and cognitive tasks.

Bibliography

[1] L. D. Lord, A. B. Stevner, G. Deco, and M. L. Kringelbach, "Understanding principles of integration and segregation using whole-brain computational connectomics: Implications for neuropsychiatric disorders," *Philos. Trans. R. Soc. A Math. Phys. Eng. Sci.*, vol. 375, no. 2096, 2017, doi: 10.1098/rsta.2016.0283.

[2] E. W. Lang, A. M. Tomé, I. R. Keck, J. M. Górriz-Sáez, and C. G. Puntonet, "Brain connectivity analysis: A short survey," *Comput. Intell. Neurosci.*, vol. 2012, no. iii, 2012, doi: 10.1155/2012/412512.

[3] O. Sporns, G. Tononi, and R. Kötter, "The human connectome: A structural description of the human brain," *PLoS Comput. Biol.*, vol. 1, no. 4, pp. 0245–0251, 2005, doi: 10.1371/journal.pcbi.0010042.

[4] K. J. Friston, "Functional and effective connectivity in neuroimaging: A synthesis," *Hum. Brain Mapp.*, vol. 2, no. 1–2, pp. 56–78, 1994, doi: 10.1002/hbm.460020107.

[5] H. Johansen-Berg and M. F. S. Rushworth, "Using Diffusion Imaging to Study Human Connectional Anatomy," 2009, doi: 10.1146/annurev.neuro.051508.135735.

[6] S. Lim, C. E. Han, P. J. Uhlhaas, M. Kaiser, and P. Uhlhaas, "Preferential Detachment During Human Brain Development: Age-and Sex-Specific Structural Connectivity in Diffusion Tensor Imaging (DTI) Data," 2013, doi: 10.1093/cercor/bht333.

[7] C. Koè, R. Apps, I. Bechmann, J. L. Lanciego, J. Mey, and S. Thanos, "Current concepts in neuroanatomical tracing." [Online]. Available: www.elsevier.com/locate/pneurobio.

[8] P. L. Nunez *et al.*, "EEG coherency I: statistics, reference electrode, volume conduction, Laplacians, cortical imaging, and interpretation at multiple scales," 1997.

[9] M. J. Brookes *et al.*, "Measuring functional connectivity using MEG: Methodology and comparison with fcMRI," 2011, doi: 10.1016/j.neuroimage.2011.02.054.

[10] K. J. Friston, C. D. Frith, P. F. Liddle, and R. S. J. Frackowiak, "Functional Connectivity: The Principal-Component Analysis of Large (PET) Data Sets," *J. Cereb. Blood Flow Metab.*, vol. 13, pp. 5–14, 1993.

[11] A. Gardner *et al.*, "Towards mapping the brain connectome in depression: Functional connectivity by perfusion SPECT," 2014, doi: 10.1016/j.pscychresns.2014.05.008.

[12] V. G. van de Ven, E. Formisano, D. Prvulovic, C. H. Roeder, D. E. Linden, and D. Linden, "Functional Connectivity as Revealed by Spatial Independent Component Analysis of fMRI Measurements During Rest," *Hum. Brain Mapp.*, vol. 22, pp. 165–178, 2004, doi: 10.1002/hbm.20022.

[13] J. Kang, F. Zou, M. A. Lindquist, and Y. Xu, “Dynamic connectivity detection: an algorithm for determining functional connectivity change points in fMRI data,” *Front. Neurosci. | www.frontiersin.org*, vol. 9, p. 285, 2015, doi: 10.3389/fnins.2015.00285.

[14] M. D. Fox and M. E. Raichle, “Spontaneous fluctuations in brain activity observed with functional magnetic resonance imaging,” *Nat. Rev. Neurosci.*, vol. 8, no. 9, pp. 700–711, Sep. 2007, doi: 10.1038/NRN2201.

[15] J. V. Cramer, B. Gesierich, S. Roth, M. Dichgans, M. Düring, and A. Liesz, “In vivo widefield calcium imaging of the mouse cortex for analysis of network connectivity in health and brain disease,” *Neuroimage*, vol. 199, no. November 2018, pp. 570–584, 2019, doi: 10.1016/j.neuroimage.2019.06.014.

[16] K. Mann, C. L. Gallen, and T. R. Clandinin, “Whole-Brain Calcium Imaging Reveals an Intrinsic Functional Network in Drosophila,” *Curr. Biol.*, vol. 27, no. 15, pp. 2389-2396.e4, 2017, doi: 10.1016/j.cub.2017.06.076.

[17] L. Avitan *et al.*, “Spontaneous Activity in the Zebrafish Tectum Reorganizes over Development and Is Influenced by Visual Experience,” *Curr. Biol.*, vol. 27, no. 16, pp. 2407-2419.e4, 2017, doi: 10.1016/j.cub.2017.06.056.

[18] C. Diaz Verdugo *et al.*, “Glia-neuron interactions underlie state transitions to generalized seizures,” *Nat. Commun. 2019 101*, vol. 10, no. 1, pp. 1–13, Aug. 2019, doi: 10.1038/s41467-019-11739-z.

[19] W. D. Penny, K. J. Friston, J. T. Ashburner, S. J. Kiebel, and T. E. Nichols, *Statistical Parametric Mapping: The Analysis of Functional Brain Images*. Elsevier Science & Technology.

[20] A. Abou Elseoud, “Group-ICA model order highlights patterns of functional brain connectivity,” doi: 10.3389/fnsys.2011.00037.

[21] K. J. Worsley, J.-I. Chen, J. Lerch, and A. C. Evans, “Comparing functional connectivity via thresholding correlations and singular value decomposition,” doi: 10.1098/rstb.2005.1637.

[22] D. Cordes, V. Haughton, J. D. Carew, K. Arfanakis, and K. Maravilla, “Hierarchical clustering to measure connectivity in fMRI resting-state data,” 2002.

[23] C. Windischberger *et al.*, “Fuzzy Diagnostic and Therapeutic Decision Support, O ¨ sterreichische Computer Gesellschaft,” pp. 111–118, 2000, Accessed: Aug. 12, 2021. [Online]. Available: http://www.fil.ion.ac.uk/spm.

[24] M. Van Den Heuvel, R. Mandl, and H. H. Pol, “Normalized Cut Group Clustering of Resting-State fMRI Data,” doi: 10.1371/journal.pone.0002001.

[25] A. Roebroeck, E. Formisano, and R. Goebel, “The identification of interacting networks in the brain using fMRI: Model selection, causality and deconvolution,” 2011, doi: 10.1016/j.neuroimage.2009.09.036.

[26] K. J. Friston, L. Harrison, and W. Penny, “Dynamic causal modelling,” 2003, doi: 10.1016/S1053-8119(03)00202-7.

[27] V. Essen and G. Tononi, *An Introduction to Brain Networks*. 2016.

[28] Y. He and A. Evans, "Graph theoretical modeling of brain connectivity," *Curr. Opin. Neurol.*, vol. 23, no. 4, pp. 341–350, 2010, doi: 10.1097/WCO.0b013e32833aa567.

[29] E. Bullmore and O. Sporns, "Complex brain networks: Graph theoretical analysis of structural and functional systems," *Nat. Rev. Neurosci.*, vol. 10, no. 3, pp. 186–198, 2009, doi: 10.1038/nrn2575.

[30] D. T. C. Edward D. Levin, "Behavioral Neuroscience of Zebrafish," in *Methods of Behavior Analysis in Neuroscience*, .

[31] G. R. Garcia, P. D. Noyes, and R. L. Tanguay, "Advancements in zebrafish applications for 21st century toxicology," 2016, doi: 10.1016/j.pharmthera.2016.03.009.

[32] K. Howe *et al.*, "The zebrafish reference genome sequence and its relationship to the human genome," 2013, doi: 10.1038/nature12111.

[33] R. Spence, G. Gerlach, C. Lawrence, and C. Smith, "The behaviour and ecology of the zebrafish, Danio rerio," *Biol. Rev*, vol. 83, no. 13, pp. 13–34, 2008, doi: 10.1111/j.1469-185X.2007.00030.x.

[34] C. Wyatt, E. M. Bartoszek, and E. Yaksi, "Methods for studying the zebrafish brain: Past, present and future," *Eur. J. Neurosci.*, vol. 42, no. 2, pp. 1746–1763, Jul. 2015, doi: 10.1111/EJN.12932.

[35] O. R. Braubach, H.-D. Wood, S. Gadbois, A. Fine, and R. P. Croll, "Olfactory conditioning in the zebrafish (Danio rerio)," *Behav. Brain Res.*, vol. 198, pp. 190–198, 2009, doi: 10.1016/j.bbr.2008.10.044.

[36] M. B. Orger, M. C. Smear, S. M. Anstis, and H. Baier, "Perception of Fourier and non-Fourier motion by larval zebrafish," 2000, Accessed: Aug. 17, 2021. [Online]. Available: http://neurosci.nature.com.

[37] K. P. Mueller and S. C. F. Neuhauss, "Quantitative measurements of the optokinetic response in adult fish," *J. Neurosci. Methods*, vol. 186, pp. 29–34, 2010, doi: 10.1016/j.jneumeth.2009.10.020.

[38] G. Pradel, M. Schachner, and R. Schmidt, "Inhibition of Memory Consolidation by Antibodies against Cell Adhesion Molecules after Active Avoidance Conditioning in Zebrafish," 1999.

[39] M. Sison and R. Gerlai, "Associative learning in zebrafish (Danio rerio) in the plus maze," *Behav. Brain Res.*, vol. 207, pp. 99–104, 2010, doi: 10.1016/j.bbr.2009.09.043.

[40] P. Lal *et al.*, "Identification of a neuronal population in the telencephalon essential for fear conditioning in zebrafish," doi: 10.1186/s12915-018-0502-y.

[41] T. Mueller, "What is the thalamus in zebrafish?," *Front. Neurosci.*, vol. 6, no. MAY, pp. 1–14, 2012, doi: 10.3389/fnins.2012.00064.

[42] A. B. Butler and W. Hodos, *Comparative Vertebrate Neuroanatomy: Evolution and Adaptation*. Wiley-Liss, 2005.

[43] P. Lal *et al.*, "Identification of a neuronal population in the telencephalon essential for fear conditioning in zebrafish," *BMC Biol.*, vol. 16, no. 1, pp. 1–18, 2018, doi: 10.1186/s12915-018-0502-y.

[44] S. Fore, F. Palumbo, R. Pelgrims, and E. Yaksi, "Information processing in the vertebrate habenula," *Semin. Cell Dev. Biol.*, 2017, doi: 10.1016/j.semcdb.2017.08.019.

[45] I. H. Bianco and S. W. Wilson, "The habenular nuclei: A conserved asymmetric relay station in the vertebrate brain," *Philos. Trans. R. Soc. B Biol. Sci.*, vol. 364, no. 1519, pp. 1005–1020, 2009, doi: 10.1098/rstb.2008.0213.

[46] N. Jurisch-Yaksi, E. Yaksi, and C. Kizil, "Radial glia in the zebrafish brain: Functional, structural, and physiological comparison with the mammalian glia," *Glia*, vol. 68, no. 12, pp. 2451–2470, 2020, doi: 10.1002/glia.23849.

[47] E. M. Bartoszek *et al.*, "Ongoing habenular activity is driven by forebrain networks and modulated by olfactory stimuli," *Curr. Biol.*, pp. 1–14, 2021, doi: 10.1016/j.cub.2021.08.021.

[48] R. K. P. Benninger and D. W. Piston, "Two-photon excitation microscopy for unit 4.11 the study of living cells and tissues," *Curr. Protoc. Cell Biol.*, no. SUPPL.59, pp. 1–24, 2013, doi: 10.1002/0471143030.cb0411s59.

[49] J. SK, V.-L. N, and Y. E, "Spontaneous activity governs olfactory representations in spatially organized habenular microcircuits," *Curr. Biol.*, vol. 24, no. 4, pp. 434–439, Feb. 2014, doi: 10.1016/J.CUB.2014.01.015.

[50] V. N *et al.*, "Light-sheet functional imaging in fictively behaving zebrafish," *Nat. Methods*, vol. 11, no. 9, pp. 883–884, 2014, doi: 10.1038/NMETH.3040.

[51] L. M. Barnett, T. E. Hughes, and M. Drobizhev, "Deciphering the molecular mechanism responsible for GCaMP6m's Ca2+-dependent change in fluorescence," *PLoS One*, vol. 12, no. 2, p. e0170934, Feb. 2017, doi: 10.1371/JOURNAL.PONE.0170934.

[52] F. Kermen, P. Lal, N. G. Faturos, and E. Yaksi, "Interhemispheric connections between olfactory bulbs improve odor detection," *PLOS Biol.*, vol. 18, no. 4, p. e3000701, Apr. 2020, doi: 10.1371/JOURNAL.PBIO.3000701.

[53] R. I *et al.*, "Motile-Cilia-Mediated Flow Improves Sensitivity and Temporal Resolution of Olfactory Computations," *Curr. Biol.*, vol. 27, no. 2, pp. 166–174, Jan. 2017, doi: 10.1016/J.CUB.2016.11.036.

[54] S. Mimaroglu and E. Erdil, "Combining multiple clusterings using similarity graph," *Pattern Recognit.*, vol. 44, pp. 694–703, 2010, doi: 10.1016/j.patcog.2010.09.008.

[55] U. Von Luxburg, "A tutorial on spectral clustering," *Stat. Comput.*, vol. 17, no. 4, pp. 395–416, 2007, doi: 10.1007/s11222-007-9033-z.

[56] F. Chung, *Spectral graph theory*. 1997.

[57] B. Mohar, “The Laplacian spectrum of graphs,” in *Graph theory, combinatorics, and applications. Vol. 2*, 1991, pp. 871–898.

[58] B. Mohar, “Some Applications of Laplace Eigenvalues of Graphs.”

[59] R. Quinlan, “Spectral Graph Theory MA500-1: Lecture Notes Semester 1 2016-2017,” 2017.

[60] W. N. Anderson, T. D. Morley, and J. R. And, “Eigenvalues of the Laplacian of a graph , Linear and Multilinear Algebra,” *L~neczr anti Multdinrur Algehim*, vol. 18, no. 2, pp. 141–145, 1985, doi: 10.1080/03081088508817681.

[61] A. Y. Ng and M. I. Jordan, “On Spectral Clustering: Analysis and an algorithm.”

[62] J. Shi and J. Malik, “Normalized cuts and image segmentation,” *IEEE Trans. Pattern Anal. Mach. Intell.*, vol. 22, no. 8, pp. 888–905, 2000, doi: 10.1109/34.868688.

[63] B. Beckman, *Theory of Spectral Graph Layout*. Tech. Report MSR-TR-94-04, Microsoft Research, 1994.

[64] Y. Koren, “Drawing graphs by eigenvectors: Theory and practice,” *Comput. Math. with Appl.*, vol. 49, no. 11–12, pp. 1867–1888, 2005, doi: 10.1016/j.camwa.2004.08.015.

[65] K. M. Hall, “An r-Dimensional Quadratic Placement Algorithm,” *Manage. Sci.*, vol. 17, no. 3, pp. 219–229, 1970, doi: 10.1287/mnsc.17.3.219.

[66] T. H. Cormen Charles E Leiserson Ronald L Rivest Clifford Stein and Y. San Francisco St Louis, “Introduction to Algorithms, Second Edition,” 2001.

[67] B. Golden, “Technical Note-Shortest-Path Algorithms: A Comparison,” 1976, doi: 10.1287/opre.24.6.1164.

[68] J. L. Hintze and R. D. Nelson, “Violin Plots: A Box Plot-Density Trace Synergism,” *Source Am. Stat.*, vol. 52, no. 2, pp. 181–184, 1998, [Online]. Available: http://www.jstor.org/stable/2685478%5Cnhttp://www.jstor.org/%5Cnhttp://www.jstor.org/action/showPublisher?publisherCode=astata.%5Cnhttp://www.jstor.org.

[69] S. Zhou, Z. Xu, and F. Liu, “Method for Determining the Optimal Number of Clusters Based on Agglomerative Hierarchical Clustering,” *IEEE Trans. Neural Networks Learn. Syst.*, vol. 28, no. 12, pp. 3007–3017, Dec. 2017, doi: 10.1109/TNNLS.2016.2608001.

[70] A. Mur, R. Dormido, N. Duro, S. Dormido-Canto, and J. Vega, “Determination of the optimal number of clusters using a spectral clustering optimization,” *Expert Syst. Appl.*, vol. 65, pp. 304–314, Dec. 2016, doi: 10.1016/J.ESWA.2016.08.059.

[71] M. Afzalan and F. Jazizadeh, “An automated spectral clustering for multi-scale data,” *Neurocomputing*, vol. 347, pp. 94–108, Jun. 2019, doi: 10.1016/J.NEUCOM.2019.03.008.

[72] J. Friedrich, P. Zhou, and L. Paninski, “Fast online deconvolution of calcium imaging data,” *PLOS Comput. Biol.*, vol. 13, no. 3, p. e1005423, Mar. 2017, doi: 10.1371/JOURNAL.PCBI.1005423.